2021

Multidisciplinary and Multi-Objective Optimal Design of a Cascade Control System for a Flexible Wing with Embedded Control Surfaces Having Actuator Dynamics

Christopher Stephen Greer

MULTIDISCIPLINARY AND MULTI-OBJECTIVE OPTIMAL DESIGN OF A CASCADE CONTROL SYSTEM FOR A FLEXIBLE WING WITH EMBEDDED CONTROL SURFACES HAVING ACTUATOR DYNAMICS

A thesis submitted to
the Graduate College of
Marshall University
In partial fulfillment of
the requirements for the degree of
Master of Science
In
Mechanical Engineering
by
Christopher Stephen Greer
Approved by
Dr. Yousef Sardahi, Committee Chairperson
Dr. Mehdi Esmaeilpour
Dr. Xia Hua

Marshall University
May 2021

APPROVAL OF THESIS

We, the faculty supervising the work of Christopher Stephen Greer, affirm that the thesis titled

*"MULTIDISCIPLINARY AND MULTI-OBJECTIVE OPTIMAL DESIGN OF A CASCADE

CONTROL SYSTEM FOR A FLEXIBLE WING WITH EMBEDDED CONTROL SUFACES

HAVING ACTUATOR DYNAMICS"*, meets the high academic standards for original scholarship and

creative work established by the Master of Science in Mechanical Engineering and the College of

Engineering and Computer Sciences. This work also conforms to the editorial standards of our discipline

and the Graduate College of Marshall University. With our signatures, we approve the manuscript for

publication.

Dr. Yousef Sardahi   Committee Chairperson   Date

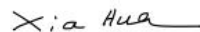   12-11- 2020

Dr. Mehdi Esmaeilpour   Committee Member   Date

                                                                    12,11,2020

Dr. Xia Hua   Committee Member   Date

                                                                    12/11/2020

ii

ACKNOWLEDGMENTS

I would like to express my gratitude to all those who helped me during the writing of this thesis. I gratefully acknowledge the help of my advisor, Dr. Yousef Sardahi, who has offered me valuable suggestions in my academic studies and has guided me though my master's program as well as an Air Force Fellowship. Without his kind support and guidance this accomplishment would not have been possible.

Second, I would like to express my heartfelt gratitude to my thesis committee: Dr. Mehdi Esmaeilpour and Dr. Xia Hua, for their instruction and assistance.

As well, I would like to thank my family for their continuous support and encouragement. Without their trust and help, I could not have the strong motivations to urge me working hard on this thesis.

Finally, I would like to thank NASA whom through the grant #80NSSC19M0054 and the Wright Patterson Air Force Base for the opportunities through grants and a summer fellowship this research would not have been possible. A special thanks to Dr. Raymond Kolonay who was Dr. Sardahi and my advisor at the Wright Patterson Air Force Fellowship. This research is supported in part by the AFRL/DAGSI Student-Faculty Fellowship program 2019-2020 and the Air Force Summer Faculty Fellowship Program (AFRL/SFFP), 2020.

TABLE OF CONTENTS

LIST OF TABLES

LIST OF FIGURES

ABSTRACT

A multidisciplinary and multi-objective optimization approach that integrates the design of the control surfaces' sizes, active control systems, and estimator for an aircraft's wing with three control surfaces is developed. Due to its attractive stability robustness properties, a control system based on the LQR (Linear Quadratic Regulator) is built for each control surface. The geometrical parameters of the control surfaces such as the span wise and chord lengths, the design details of the LQR penalty matrices, and the locations of the estimator poles are tuned by a widely used multi-objective optimization algorithm called NSGA-II (Non-dominated Sorting Genetic Algorithm). Four objectives are considered: minimizing impacts of external gust loads, maximizing stability robustness and extending flutter boundaries, reducing control energy consumption, and minimizing the Frobenius norm of the estimator gains. The solution of the multi-objective optimization problem is a set called Pareto set and the set of the corresponding function evaluation is called Pareto front. The solution set contains various geometrical configurations of the control surfaces with different feedback gains, which represent different degrees of optimal compromises among the design objectives. The optimization results demonstrate the competing relationship between the design objectives and necessity of handling the design problem in a multidisciplinary and multi-objective context. Three major results are obtained from inspecting the profiles of the closed-loop eigenvalues at various airspeeds 1) a unique control gain can be designed for the entire flight envelope, 2) the flutter boundaries can be infinitely extended, and 3) a unique observer gain can be designed for the entire flight envelope. The third chapter of this thesis presents a multi-objective and multidisciplinary optimal design of a cascade control system for an aircraft wing with four aerodynamic ailerons actuated by four identical brushless DC motors. The design of the control system is broken into a

secondary and primary control algorithm. The primary control algorithm is designed based on the concept of LQR and then applied to mathematical model of the wing and its control surfaces to calculate their required deflections. The output of the primary controller serves as set-point for the secondary control loop which consists of the dynamic of the DC motor and Proportional Velocity (PV) based controller. Then, an optimal design of the control algorithms is carried out in multi-objective and multidisciplinary settings. Three objectives are considered: 1) the speed of response of the secondary controlled system must be faster than that of the primary one, 2) the controlled system must be robust against external disturbances affecting both control layers, and 3) optimal energy consumption. The decision variables of the primary as well as secondary control algorithms and the sizing elements of the control surfaces form the design parameter space of the optimization problem. Both geometrical and dynamic constraints are applied on the setup parameters. The multi-objective optimization problem (MOP) is solved by NSGA-II, which is one of the popular algorithms in solving MOPs. The solution of the MOP is a set of optimal control algorithms that represent the conflicts among the design objectives. Numerical simulations show that the design goals are achieved, the secondary control is always fast enough to prevent the propagation of disturbances to the primary loop, the inner and outer control algorithms are robust against disturbance inputs, and the primary control loop stays stable when the air stream velocity varies from 80 to 1000 (m/s) even at its worst relative stability value. The presented study may become the basis for multi-objective and multidisciplinary optimal design for aeroelastic structure having actuator dynamics.

CHAPTER 1: INTRODUCTION

1.1 Literature Review

Multidisciplinary design of flexible structures such as aircraft wings has helped improve their performance in the past. During the design, wing's geometrical parameters and control gains are varied to simultaneously satisfy multiple and often conflicting requirements. Design objectives such as maximizing the stability of the aeroelastic structures, suppression of instabilities, robustness against gust loads and measurement noise, and minimizing energy consumption are critically important when designing active aeroelastic controls (Singh, McDonough, Kolonay, and Cooper, 2014). Therefore, additional work on the subject can further improve their performance by combining the concept of multidisciplinary design with that of multi-objective optimization.

There have been a few research efforts in the field of multidisciplinary optimal design of aircraft wings. Khot and his colleagues optimized a realistic wing with constraints on the strength and frequency distribution and obtained a feasible flexible wing structure (Khot, Appa, and Eastep, 2000). Then, the structure design was utilized in an optimal controller design to determine the actuator force distribution. Several articles have optimized wing control surface sizing using a MATLAB optimization toolbox feature, constrained optimization solver, simultaneously calculating control gains for receptance-based control Singh and McDonough (2014); Brown and Singh (2015); Brown, Singh and Kolonay (2017). Specifically, Singh et al. (2014) developed two optimization problems. The first problem used the control surface chord length of a wing with a single control surface as a parameter. In the second problem, the span wise length of the first control surface of a wing with multiple control surfaces was chosen as a variable. In both problems the objective was to minimize the control system energy through

1

minimization of the norms of the control gains satisfying some constraints of closed-loop poles; these poles define the extension of the open loop flutter boundary. Whereas in Brown and Singh (2015), the span wise lengths, locations, and chord sizes of a leading and trailing control surface were tuned to satisfy static constraints regarding the size of the control surfaces, in addition to dynamic constraints related to the active pole placement for flutter boundary extension. Alternatively, Brown et al. (2017) implemented genetic algorithms to tune the location, size, and number of leading and trailing control surfaces for a fighter wing model. The main goal was to achieve optimized aeroelastic control of flutter boundary extension with minimum control effort, leading to two cases being considered. The first case had a fixed number of control surfaces while chords, span lengths, and locations were tuned. The second case tuned the number and locations of control surfaces while their sizes were both fixed. Both geometrical static and dynamic constraints were applied for optimization.

The combination of multidisciplinary design-optimization approaches and wing aerostructure design with control-system design was implemented (Stanford, 2016; Nam, Chattopadhyay, and Kim, 2000; Haghighat, Martins, and Liu, 2012). A series of aeroelastic optimization problems under a variety of static and dynamic aeroelastic constraints was solved, (Stanford, 2016). One such optimization problem, the wing mass was minimized by tuning structural variables such as skin thickness and stiffener details, the quasi-steady deflection scheduling of a series of control surface distributed along the trailing edge for maneuver load alleviation and trim attainment. Nam et al. (2000) utilizes genetic algorithms for an integrated simultaneous aeroservoelastic design of a composite wing. Variables such as ply orientation of the composite layer, wing sweep angle, taper ratio, span wise location and size of control surfaces were chosen as design parameters for the genetic algorithm. A weighted sum of 25

index values was defined as the objective function, which represents the LQR performance index based on output feedback controller airspeed and the root mean square values of the gust response at various airspeeds. The outcome of this work showed improvements when compared to baseline models. In Haghighat et al. (2012), the main design goal was to maximize the endurance of a high-altitude long-endurance aircraft by tuning win planform parameters, structural sizing, and control gains simultaneously. The results showed the simultaneous design of the control system along with structural components of wings at early stage of design improves aircraft performance.

Multidisciplinary design of aircraft wings with active flight control systems has helped improve wing performance in the past. In this kind of design, wing geometrical parameters and control gains are tuned to simultaneously achieve multiple and often conflicting criteria. Design requirements include, but are not limited to, suppression of instabilities and extension of flutter boundaries, robustness against gust loads and measurement noises, and minimization of energy consumption (Singh et al., 2014). Therefore, additional work on the subject can further improve the performance of aerospace structures by combining the concept of multidisciplinary design with that of multi-objective optimization. The need of multidisciplinary design optimization (MDO) was extensively discussed by Livne and Jackson (Livne, 1999), (Jackson and Livne, 2014).

Optimization of aeroelastic structures has been addressed in several papers. For instance, (Karpel and Sheena, 1989) used a computer program to optimally resize a wing structure and achieve a maximum control effectiveness with minimum weight increase. Sizes of upper skin and lower skin were factored as design parameters. Pettit (Pettit and Grandhi, 2003) used a gradient-based optimization algorithm to optimize a fighter-like wing modeled with finite

elements. The mean thickness values of the wing's elements were tuned to alleviate gust response and improve aileron effectiveness. Vio and Cooper (2008) made use of evolutionary algorithms to reduce the impact of passive gust loads on a typical commercial aircraft wing by tuning the orientation and thickness of the layers in the composite layup. The optimization process was repeated for different combinations of objectives such as maximizing flutter speed and minimizing the wing's mass, maximizing the flutter speed via thickness at base model, and minimizing the maximum gust response while minimizing mass concurrently. In similar fashion, genetic algorithms were utilized to enhance the aerodynamic performance of a wing used on the RQ-7 Shadow UAV (Ahuja and Hartfield, 2010). Specific design variables were chosen such as chord span, dihedral angles, and inclination angle; then a cost function was created by aggregating three objectives: minimum wing weight, maximum lift, and minimum drag. Nikbay and Acar (2012) showed through the optimal design of an AGARD wing and changing structural parameters such as taper ratio, sweep angle, elasticity, and shear modulus etc. that the flutter boundaries of the structure can be extended. Boopathy, Rumpfkeil, and Kolonay (2015) proposed robust and optimal structural sizing of a fighter wing configuration under both structural and material uncertainties. The weight of the wing was minimized through adjusting the cross-section area and thickness of structural members. Kim, Jeon, and Lee (2006) introduced a multi-objective design optimization of supersonic fighter wing. The wing's planform parameters such as the sweep angle, aspect ratio, linear twist angle, area, and taper ratio; airfoil shapes setup knobs such as the thickness ratio, maximum camber of the airfoil at the wing root, and thickness ratio, and maximum camber of airfoil at the wing tip; and four parameters related to the structural skin thickness of the wing were tuned by the response surface

4

method and genetic algorithm. A weighted sum of the wing weight, drag, and/or lift-to-drag ratio was used as a design objective.

Multidisciplinary design of flexible structures has been reported in several manuscripts. For example, an MDO of an aircraft wing was investigated by Khot et al. (2000) to enhance the wing roll performance at a high dynamic pressure. The structure of the wing was optimized first to obtain a feasible flexible wing. Then, an optimal control design was conducted to determine the distribution of actuator forces. Singh and McDonough (2014) formulated two optimization problems. In the first problem, the chord fraction of an aileron attached to a wing was selected as a variable. In the second problem, only the span-wise length of the first control surface of a wing having multiple control surfaces was selected as a design variable. In both problems, the optimization goal was to minimize the control system energy through minimizing the norms of the control gains while satisfying some constraints on closed-loop poles, which define the extension of the open loop flutter boundary. Likewise, Brown and Singh (2015) optimally adjusted the locations, span wise lengths, and chord sizes of a leading and trailing edge control surface under static constraints related to the size of the control surfaces as well as dynamic constraints related to the active pole placement for flutter boundary extension. In another study, Brown et al. (2017) used genetic algorithms to tune the size, location, and number of leading and trailing control surfaces of a fighter wing model. The optimization goal was to achieve an active aeroelastic control for flutter boundary extension with minimum control effort. Therein, two cases were considered. In the first optimization problem, the number of control surfaces were fixed while their chords, span lengths, and locations were tuned. In the second optimization problem, the number and locations of control surfaces were tuned while their sizes were fixed. Stanford (2016) solved a series of aeroelastic optimization problems for a subsonic transport

wing under a variety of static and dynamic aeroelastic constraints. In one of these optimization problems, the mass of the wing was minimized by simultaneously tuning structural variables (skin thickness, stiffener details), the quasi-steady deflection scheduling of a series of control surfaces distributed along the trailing edge for maneuver load alleviation and trim attainment, and the design details of a Linear Quadratic Regulator (LQR). By the same token, Nam and his co-authors (2000) employed genetic algorithms for an integrated simultaneous aeroservoelastic design of a composite aircraft wing. Eight design variables consisting of ply orientation of the composite layer, wing sweep angle, taper ratio, aspect ratio, span wise location and size of the control surfaces were selected as design parameters. The objective function was defined as a weighted sum of 25 index values, which are LQR performance index based on an output feedback controller at a design airspeed and the root mean square values of the gust responses for various airspeeds. The results showed considerable improvements in both objectives when the optimized models were compared to baseline models. Another MDO study was presented by Haghighat et al. (2012). Therein, the main design goal was to maximize the endurance of a high-altitude long endurance aircraft by tuning wing planform parameters (wing area and span-wise twist distribution), structural sizing (spar-wall thicknesses), and control gains (diagonal elements of the state weighting matrix of the LQR algorithm) concurrently. The results showed the simultaneous design of the control system along with structure of the wing at the early stages of aircraft design improves aircraft performance.

In all the aforementioned studies, the dynamics of the actuators driving the control surfaces was ignored. It is well-known that implementing an active aeroelastic control on a given wing needs actuators. The dynamics of the actuators has great influence on the overall system performance. The first attempt toward including actuators' dynamics in the control system

design was in 2016 (Singh, Brown, and Kolonay, 2016). Therein, a receptance-based controller was designed for a wing with a leading and trailing control surface and the control gains required to place the closed-loop poles at prescribed locations were computed by solving a set of nonlinear equations in the least-square sense. Second and third-order models of the actuator were tested and simultaneous control of aeroelastic structure and actuators were designed. However, an optimal design of cascade active aeroelastic controls for the wing, ailerons, and actuators in multi-objective and multidisciplinary settings has not been investigated yet. The cascade control design is selected because it significantly improves the performance of feedback controllers. Unlike single feedback control loops, cascade control methods can act quickly to prevent external excitations from propagating through the process and ensure the controlled variable does not deviate from its desired level (Smith and Corripio, 1985).

It is evident from the literature that genetic algorithms have been used in many studies. One of the popular genetic algorithms is the NSGA-II. The working principle of this algorithm is introduced in the next section.

1.2 NSGA-II

NSGA developed in Srinivas and Deb (1994) is a non-domination based genetic algorithm. Even though it performs well in solving MOPs, its high computational effort, lack of elitism, and the implementation of what is called sharing parameter had necessitated improvements. As a result, a modified version of the algorithm named NSGA-II was presented in Deb, Pratap, Agarwal, and Meyarivan (2002). The new version has a better sorting algorithm, includes elitism, eliminates the need for the sharing parameter, and has less computational burden. As shown in Figure 1, the algorithm incorporates eight basic operations: Initialization,

fitness evaluation, non-domination ranking, crowding distance calculation, tournament selection, crossover, mutation, and combination (Deb et al., 2002).

The algorithm starts with the initialization process in which a random population, *Npop*, that satisfies the lower and upper bound constraints is generated. Once the population is initialized, fitness function evaluations, *F(Pop)*, takes place in the second stage. Using these function values, the candidate solutions are sorted based on their non-domination and placed into different fronts. The solutions in the first front dominate all the other individuals while those in the second front are dominated only by the members in the first front. Similarly, the solutions in the third front are dominated by individuals in both the first and second fronts, and so on. Each candidate solution is given a rank number, *rnk*, of the front where it resides. For instance, members in first front are ranked 1 and those in second are given a rank of 2 and so on.
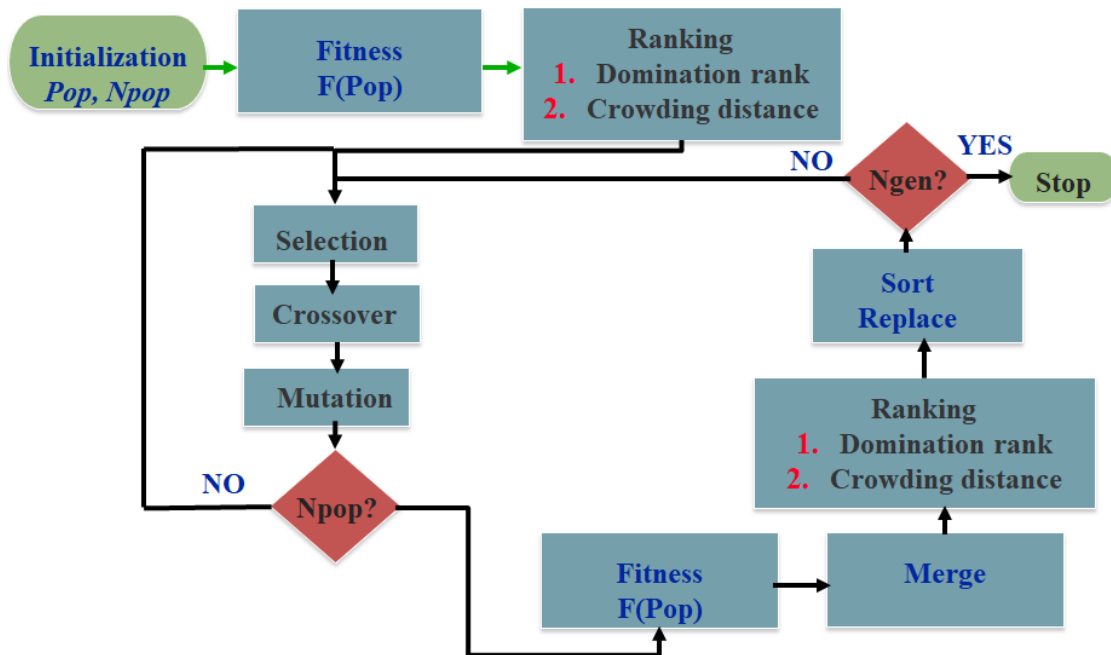
Figure 1: *NSGA-II algorithm flowchart*

To improve the diversity of the solution, a parameter called the crowding distance is computed for each solution. This parameter measures how close an individual is to its neighbors. The crowding distance is calculated front wise since comparing the crowding distance between two individuals from two different fronts is meaningless. The larger the average crowding distance, the better the diversity of the population. After that, the parents for the next generation are selected. One of the popular algorithms used for this purpose is the binary tournament selection method. At each iteration $i = 1 : n_c$, where $n_c = round(Npop = 2)$ and n_c is the number of parents, two random integer numbers are uniformly generated between 1 and $Npop$. These values are used to fetch two candidate parents from Pop. A candidate solution is selected if its rank is smaller than the other or if its diversity measure is bigger than the other. Then, a crossover algorithm such as the arithmetic crossover method (Beyer and Deb, 2001; Deb and Agrawal, 1995) and a mutation algorithm such as the simple mutation approach (Kakde, 2004) are applied on the selected parents to produce new children. These two operations are repeated *nc* times which result in a new offspring of size $Npop$. Elaborated details about crossover and mutation methods can be found in Haupt and Ellen Haupt (2004). After that, the new children are merged with the current population. This combination guarantees the elitism of the best individuals. Finally, individuals are sorted based on their crowding distance and rank values. First, the sorting is performed with respect to the crowding distance in a descending order. Then, an ascending order of the population is followed based on the rank values. The new generation is produced from the sorted population until the size reaches $Npop$. As long as the number of generations, *gen*, is not equal to the maximum number of iterations, *Ngens*, the selection, crossover, mutation, merging, ranking and sorting process are repeated.

9

NSAG-II works well on two-objective and three-objective problems. For many-objective optimization problems (with more than three objectives), large populations are used to enhance the search ability of the algorithm but at the expense of the computation time (Shibuchi, Sakane, Tsukamoto, and Nojima, 2009). A study on the effect of the size of the decision variable space on the performance of NSGA-II and other evolutionary algorithms showed that NSGA-II converges to the true Pareto front on all the test problems when the number of design parameters is less than or equal to 128 (Durillo, Nebro, Coello, Luna, and Alba, 2008; Durillo et al., 2010). In this, the size of the objective space is 4 and that of decision variable space is between 4 and 10. Therefore, NSGA-II is expected to perform well in these two problems.

1.3 Outline of the Thesis

This thesis is based on the author's research on multidisciplinary optimal design of an active control system and state estimator for an aircraft wing and multidisciplinary and multi-objective optimal design of a cascade control system for a flexible wing with embedded control surfaces having actuator dynamics in the past year. Chapter 2 proposes multidisciplinary optimal design of an active control system and state estimator for an aircraft wing. The third chapter of this thesis presents a multi-objective and multidisciplinary optimal design of a cascade control system for an aircraft wing with four aerodynamic ailerons actuated by four identical brushless DC motors. Chapter 4 summarizes the thesis.

CHAPTER 2: MULTIDISCIPLINARY OPTIMAL DESIGN OF AN ACTIVE CONTROL SYSTEM AND STATE ESTIMATOR FOR AN AIRCRAFT WING

2.1 Introduction

A multidisciplinary and multi-objective optimization approach that integrates the design of the control surfaces' sizes, active control systems, and estimator for an aircraft's wing with three control surfaces is developed in this chapter. Four objectives are considered: minimizing impacts of external gust loads, maximizing stability robustness, extending flutter boundaries, reducing control energy consumption, and minimizing the Frobenius norm of the estimator gains. Wing's mathematical model, control system and observer design, formulation of the optimization problem, and discussion of the results are delineated in the next sections.

2.2 Mathematical Model of an Aircraft's Wing with Multiple Control Surfaces

Consider the flexible wing having three control surfaces shown in Figure 1. The matrix-differential equation which rules the dynamic of the system is given by

$$M\ddot{q}(t) + (C - \rho V C_a)\dot{q}(t) + (K - \rho V^2 K)q(t) = F_c u(t) + F_g w_g(t) \qquad (1)$$

The vector $\mathbf{q}(t) = [q_1(t), q_2(t), q_3(t), q_4(t)]^T$ represents the generalization coordinate, $\mathbf{u}(t) = [\beta_1(t), \beta_2(t), \beta_3(t)]^T$ denotes the vector of the control surface deflection, F_c is the matrix describing the influence of the controls on the system dynamics, and F_g describes the influence of the aerodynamic load, $w_g(t)$, on the system behavior. The matrices $\mathbf{M}$, C_a, $\mathbf{C}$, K_a, and $\mathbf{K}$ are the structural inertia, aerodynamic damping, structural damping, aerodynamic stiffness, and structural stiffness matrices, respectively. The reader can refer to Appendix C or more details about the model and the numerical values used in the simulation.
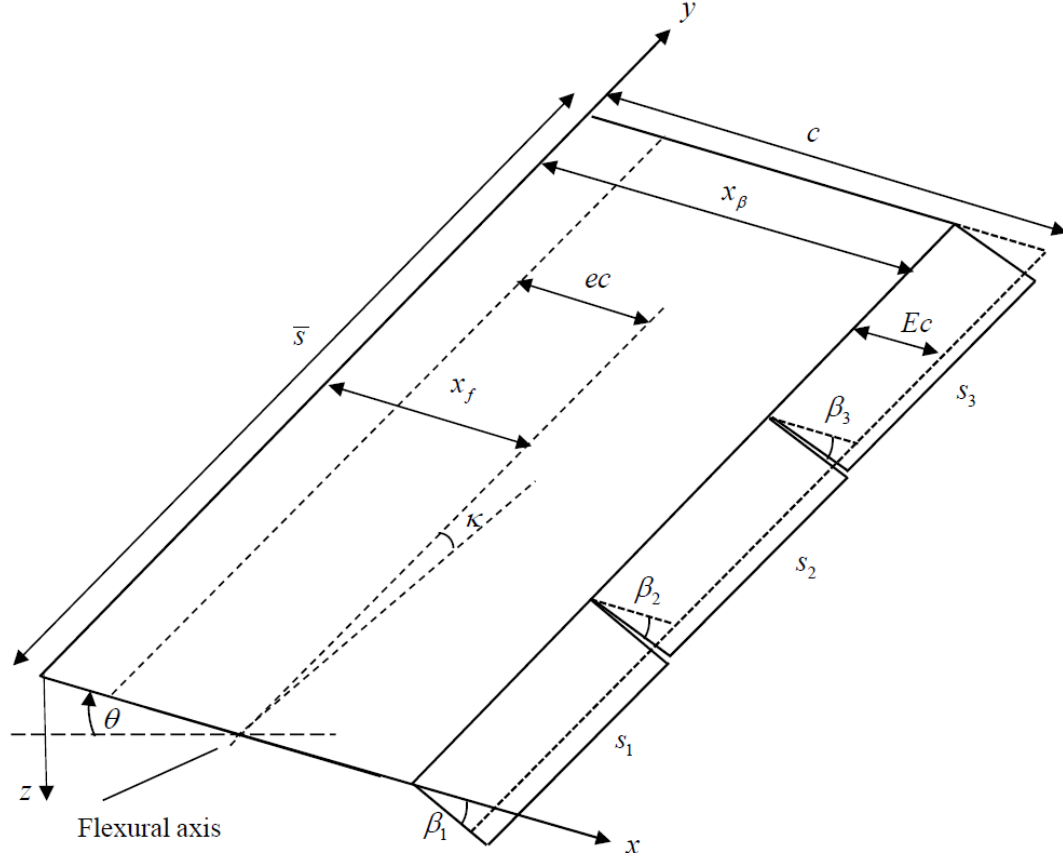
Figure 2: *Flexible aircraft wing model with three control surfaces (Singh et al., 2014)*

The bending deformation (transverse direction) z and rotation θ at a point (x, y) on the wing are related to the generalized coordinates and the wing's dimensions by the following equations:

$$z = y^2 q_1 + y^3 q_2 + y(x - x_f)q_3 + y^2(x - x_f)q_4 \tag{2}$$

$$\theta = y q_3 + y^2 q_4 \tag{3}$$

where, x_f is the flexural axis location aft of leading edge.

2.3 Optimal Full-State Feedback Control System

The state-space model of the system described in Eq. (1) reads

$$\dot{x}(t) = Ax(t) + B_u u(t) + B_g w_g(t) \qquad (4)$$

The output equation is given by

$$y(t) = C_o x(t) \qquad (5)$$

Where, $x(t) = [q_1(t), q_2(t), q_3(t), q_4(t), \dot{q}_1(t), \dot{q}_2(t), \dot{q}_3(t), \dot{q}_4(t)]^T$ is the state vector. The

system matrices A, B_u, B_g, and C_o are given by

$$A = \begin{bmatrix} 0_{4x4} & I_{4x4} \\ -M^{-1}(K - \rho V^2 K_a) & -M^{-1}(C - \rho V C_{a)} \end{bmatrix} \qquad (6)$$

$$B_u = \begin{bmatrix} 0_{4x3} \\ M^{-1}F_c \end{bmatrix} \qquad (7)$$

$$B_g = \begin{bmatrix} 0_{4x3} \\ M^{-1}F_g \end{bmatrix} \qquad (8)$$

$$C_o = [I_{4x4} \quad 0_{4x4}] \qquad (9)$$

Where, **I** and **0** denote the identity and zero matrices, respectively. It is evident from the system

configuration that the system is completely controllable. In other words, the controlled system

with the three actuators (control surfaces), shown in Figure 1, can move any state of the system

from any initial state to any other final state in a finite time interval. Also, the system is

completely observable. That is, with the on-board sensors' distribution given in Eq. (9), the first

four states can be measured directly and then used to estimate the last four states. A MIMO full-

state feedback law for the state-space system given in Eq. (4) can be written as

$$u(t) = -K_c x(t) \qquad (10)$$

where, $K_c \in R^{3x8}$ is the state feedback gain matrix. Substituting Eq. (10) into Eq. (4), the closed-

loop dynamics is given by

$$\dot{x}(t) = (A - B_u K_c)x(t) + B_g w_g(t) \tag{11}$$

Taking the Laplace of Eq. (11), we obtain

$$(sI - A + B_u K_c)X(s) = B_g W_g(s) \tag{12}$$

where, $\mathbf{X}(s)$ and $w_g(s)$ are the Laplace transforms of $\mathbf{x}(t)$ and $w_g(t)$, respectively. Using this

equation and Eq. (5), the transfer function matrix $\mathbf{GTF(s)}$ from the gust loads to the system's

outputs is provided by

$$GTF(s) = \frac{Y(s)}{W_g(s)} = C_o(sI - A + B_u K_c)^{-1}B_g. \tag{13}$$

Here, Y(s) denotes the Laplace transform of y(t). This transfer function matrix is very crucial in

the design of an aircraft's wing since one of the design requirements is to alleviate the impacts of

extreme aerodynamic loads on the system performance. It is obvious that by increasing the

values of the elements of the feedback gain matrix K_c, the gust loads' effects can be reduced.

However, this conflicts with the requirement of minimizing the control energy needed to

stabilize the system and suppress flutter.

2.4 Linear- Quadratic Regulator (LQR) Design

The state feedback gain matrix K_c plays a very important role in the performance of the

closed-loop system. This variable can be either directly tuned if the stable ranges of its elements

are known, or indirectly calculated by solving the Algebraic Riccati Equation (ARE) which

results in a Linear Quadratic Regulator (LQR). The latter is very attractive since it does not

require any stability analysis and the user only needs to adjust some weighting factors and then

numerically solve the ARE to obtain K_c that stabilizes the controlled system. In this case, K_c

minimizes the following performance index:

$$J = \int_0^\infty [x^T(t)Qx(t) + u^T(t)Ru(t)]dt, \tag{14}$$

14

where $\boldsymbol{Q} = \boldsymbol{Q}^T$ is a positive semidefinite matrix that penalizes the departure of system states from the equilibrium, and $\boldsymbol{R} = \boldsymbol{R}^T$ is a positive definite matrix that penalizes the control input. Using Lagrange multiplier-based optimization method, the optimal $\boldsymbol{K_C}$ is given by

$$\boldsymbol{K_C} = \boldsymbol{R}^{-1}\boldsymbol{B}_u^T\boldsymbol{P}. \tag{15}$$

The matrix $\boldsymbol{P} \in \mathbb{R}^{8\times3}$ can be calculated by solving the following ARE:

$$\boldsymbol{A}^T\boldsymbol{P} + \boldsymbol{PA} - \boldsymbol{Q} - \boldsymbol{PBR}^{-1}\boldsymbol{B}_u^T\boldsymbol{P} = 0 \tag{16}$$

It is evident from equations (15) and (16) that $\mathbf{Q}$ and $\mathbf{R}$ are the design knobs that greatly impact the calculation of $\boldsymbol{K_C}$ and in turn the performance of the system under control. Thus, the most important step in the design of an optimal controller using LQR is the choice of $\mathbf{Q}$ and $\mathbf{R}$ matrices. Conventionally, these matrices are elected based on the designer's experience and adjusted iteratively to obtain the desired performance. Arbitrary selection of $\mathbf{Q}$ and $\mathbf{R}$ will result in a certain system response which is not optimal in true sense (Tewari, 2002). Many efforts have been directed toward developing systematic methods for selecting the weighting matrices. For instance, Bryson presented an approach for choosing the starting values of $\mathbf{Q}$ and $\mathbf{R}$ matrices, but this method only suggests the initial values and later the coefficients are to be tuned iteratively for optimal performance (Bryson, 2018). Analytical approach of selecting the $\mathbf{Q}$ and $\mathbf{R}$ matrices for a second order crane system was developed in Oral, Çetin, and Uyar (2010). Another analytical method of calculating the $\mathbf{Q}$ and $\mathbf{R}$ matrices for a third order system represented in the control canonical form was proposed in El Hajjaji and Ouladsine (2001). Developing an analytical technique to find $\mathbf{Q}$ and $\mathbf{R}$ for high order systems such as the system at hand is very tedious if it is not possible because of the dimension of the system. Therefore, we suggest a numerical approach through using an optimization algorithm to tune these matrices such that the design goals are optimized simultaneously.

The LQR does not only guarantee the system stability but also the stability margins. This feature is very valuable for high-order dynamic systems where finding the feasible regions of the control gains are very difficult. On the other side, LQR requires that you have a good model of the system, and all the states in the system available for feedback. If not all the states are available, an observer should be used to estimate the unavailable ones. As a result, stability margins may get arbitrarily small. To avoid this situation, the estimator dynamics should be faster than the closed-loop dynamics i.e., the estimator eigenvalues should not be closer to the imaginary axis than those of the regulator. This can be done free of cost since the estimator does not require a control input (Tewari, 2002). As a result, the estimator poles can be pushed further into the left-half plan without causing concern of large control effort.

2.5 Luenberger Observer

Practically speaking, only a subset of the states is available for feedback when the control system is designed. A cost-effective approach to determine the states that are not directly measured is to design an observer, which is nothing but a computer algorithm that uses the system mathematical model, available measurements, and feedback control signals to provide an estimate of the unavailable states. Luenberger observer is one of the popular and traditional estimators that can be used for this end (Luenberger, 1964). The dynamics of the Luenberger observer of the state-space system given in Eq. (4) reads

$$x(t) = [A\hat{x}(t) + B_u u(t) + L[y(t) - \hat{y}(t)]. \qquad (17)$$

$$\hat{y}(t) = C_o \hat{x}(t) \qquad (18)$$

16

The term $L[y(t) - \hat{y}(t)]$ injects the error between measurements $x(t)$ and model predictions $\hat{x}(t)$, scaled by a user-chosen observer gain vector $L \in \mathbb{R}^{8 \times 4}$. Letting $e(t) = x(t) - \hat{x}(t)$, the error dynamics is governed by the following equation

$$e(t) = (A - LC_o)e(t) \tag{19}$$

By examining this equation, we notice that the estimation error system is asymptotically stable, $e(t) \rightarrow 0$, if we select **L** such that the eigenvalues of $(A - LC_o)$ have negative real parts. That is, we can assign the eigenvalues (i.e., speed) of the error system by selecting **L** appropriately. Furthermore, the selection of **L** comes free of cost since the estimator does not require any form of physical control effort. As a result, the eigenvalues of the estimator λ_e can be placed to the left of the fastest mode of the closed-loop, $\lambda_{c_{min}}$ system as follows

$$\lambda_e = r \times (1:8)\lambda_{c_{min}}, \tag{20}$$

where, $\lambda_{c_{min}} = min(real(A - B_u K_c))$ and $r \geq 2$ can be tuned to find the optimal trade-offs between the observer speed of response and noise amplifications, which are directly related to the values of **L**. It can be noticed that $\lambda_{c_{min}}$ is scaled by $r \times (1 : 8)$ to avoid placing the estimator poles at the same location since the pole placement can be badly conditioned if the designer picks out unrealistic pole locations (MathWork, 2020). The proposition in Eq. (20) is introduced in this thesis to avoid this situation though other setups are also possible. Then, the MATLAB command "place" can be used to calculate **L**.

2.6 Multi-Objective Optimization

Multi-objective optimization problems (MOPs) are stated as follows:

$$\min_{k \in D}\{F(k)\}, \tag{21}$$

where a design variable vector $\boldsymbol{k} = [k_1, k_2, \ldots, k_n]$ must be found to minimize a vector $F =$ $[f_1(\boldsymbol{k}), \ldots, f_m(\boldsymbol{k})]$. The domain $D \subset \mathbb{R}^n$ can in general be expressed by inequality and equality constraints:

$$D = \{\boldsymbol{k} \in \mathbb{R}^d | g_i(k) \leq 0, i = 1, \ldots, l, \\ and\ h_j(\boldsymbol{k}) = 0, j = 1, \ldots, m\} \tag{22}$$

The solution of a MOP is known as the Pareto set and its image is called the Pareto front. Therefore, the concept of dominancy (Pareto, 1971) (original edition in French in 1927) is used to define the optimal solutions. Such solutions are non-dominated to each other. Simply stated, there exists no other solutions in the entire search space which dominate any of these solutions. MOPs are solved by multi-objective optimization algorithms which can be classified as evolutionary-based and gradient-based algorithms. The reader can refer to Jones, Mirrazavi, and Tamiz (2002); Marler and Arora (2004); and Tian, Cheng, Zhang, and Jin (2017) for comprehensive survey of MOP algorithms.

Control systems' design problems are complicated and non-convex, therefore evolutionary algorithms are the methods of choice (Woźniak, 2010). They outperform classical direct and gradient-based methods which suffer from the following problems: 1) the convergence to an optimal solution depends on the initial solution supplied by the user, and 2) most algorithms tend to get stuck at a local or suboptimal solution when solving non-convex, and complex problems. On the other side, evolutionary algorithms are computationally expensive (Hu, Huang, and Wang, 2003). However, the computational cost can be justified if a more accurate solution is desired, and the optimization is conducted offline. The most widely used multi-objective optimization algorithm is the NSGA-II (Sardahi and Boker, 2018; Xu, Sardahi,

and Zheng, 2018). It yields a better Pareto front as compared to SPEA2 (strength Pareto evolutionary algorithm) and PESA-II (Pareto Envelope based Selection Algorithm).

Therefore, in this thesis, we use the NSGA-II to solve the multi-objective optimal control problem at hand. The reader can refer to Section 1.2 or (Sardahi, 2016) for more details about the working principle of this algorithm. NSAG-II works well on two-objective and three-objective problems. For many objective optimization problems (with more than three objectives), large populations are used to enhance the searchability of the algorithm but at the expense of the computation time (Ishibuchi, 2009). A study on the effect of the size of the decision variable space on the performance of NSGA-II and other evolutionary algorithms showed that NSGA-II converges to the true Pareto front on all benchmark problems when the number of design parameters is less than or equal to 128 (Durillo et al., 2008). In this work, the size of the objective space is 4 and that of decision variable space is 15. Therefore, NSGA-II is expected to perform well in solving the optimization problem at hand.

2.7 Multi-objective and Multidisciplinary Optimal Design

Three pieces of information are needed for any optimization problem. They are the tunable parameters, fitness functions, and constraints. The design parameter spaces **k** (see Equation (21)) are given by,

$$\boldsymbol{k} = [Q_1, \dots, Q_8, R_1, R_2, R_3, \alpha_1, \alpha_2, E_c, r]. \qquad (23)$$

The parameters $Q_1, \dots, Q_8$, are the values on the main diagonal of (**Q**), and $R_1, \dots, R_3$ are the elements on the main diagonal of (**R**). These variables are numerically adjusted to optimally tune $\boldsymbol{K}_C$. The span lengths and chord of the ailerons are also tuned by varying α_1, α_2, and E_c. Where α_1 and α_2 set the length of first ($s_1 = \alpha_1 \bar{s}$) and second ($s_2 = \alpha_2 \bar{s}$) aileron. Having the values of s_1 and s_2, the length of the third aileron can be simply calculated ($s_3 = \bar{s} - (s_1 + s_2)$). It

is worth noting that by changing α_1, α_2, and E_c, the size of the control surfaces is accordingly tuned. The size of the control surface decides both the amount of control energy required to derive it and the ability of the closed loop to reject external aerodynamic loads. The reader can inspect the control and gust loading influence matrices $\boldsymbol{F_c}$ and $\boldsymbol{F_g}$ (Kumar, Nair, Begum, and Tharani, 2012) to see how these geometrical parameters enter these two matrices. The variable r dictates the locations of the estimator's poles relative to the further left pole of the closed-loop system, and in turn the speed of response of the observer. These design knobs were tuned to minimize the following design objectives

$$\min_{k \in D}\{\lambda_{cmax}, \|\boldsymbol{GTF}(j\omega)\|_\infty, \|\boldsymbol{B_u K_c}\|_F, \|\boldsymbol{L}\|_F\}. \tag{24}$$

The relative stability of the controlled system is expressed by λ_{cmax}, where $\lambda_{cmax} = max(real(eig[\boldsymbol{A} - \boldsymbol{B_u K_c}]))$ represent the real parts of eigenvalues of the closed-loop dynamic matrix. Small values of λ_{cmax} indicate better stability robustness of the system under control. The fitness function $\|\boldsymbol{GTF}(j\omega)\|_\infty$ describe the disturbance rejection capability of the closed-loop system to gust loads. A general definition of $\|\boldsymbol{GTF}(j\omega)\|_\infty$ is given by

$$\|\boldsymbol{GTF}(j\omega)\|_\infty = \sup_{\omega \in [\omega_i, \omega_f]} \sigma(\boldsymbol{GTF}(j\omega)), \tag{25}$$

where σ is the largest singular value among the transfer function elements. That is, the maximum value of $\|\boldsymbol{GTF}(j\omega)\|_\infty$ is minimized. The values of ω_i and ω_f are set to 0 and 1000, respectively, as suggested in Singh et al. (2014). For a controlled system to have a good disturbance rejection, we must have $\|\boldsymbol{GTF}(j\omega)\|_\infty \ll 1$. The third objective, $\|\boldsymbol{K_c}\|_F$, is the Frobenius norm of the control matrix and it is given by

$$\|\boldsymbol{B_u K_c}\|_F = \sqrt{\sum_{j=1}^{8} \sum_{i=1}^{8} |m_{ij}|^2}, \tag{26}$$

20

where m_{ij} are the elements of feedback gain matrix, $\boldsymbol{B_u K_c}$ (refer to Eq. (10)). Generally

speaking, the minimization of this norm leads to minimization of the control energy, which is

one of the design objectives in this work. The fourth fitness function $\|\boldsymbol{L}\|_F$, is the Frobenius

norm of the estimator gain matrix and it is defined by

$$\|\boldsymbol{L}\|_F = \sqrt{\sum_{j=1}^{8}\sum_{i=1}^{4}\left|l_{ij}\right|^2}, \tag{27}$$

where l_{ij} are the elements of $\boldsymbol{L}$. Small values of this cost function leads to slow estimator

dynamics but less noise amplification, and vice versa. Therefore, it is crucial to optimize this

objective function to ensure optimal estimator performance.

The MOP in Eq. (25) was solved by tuning the elements of $\mathbf{k}$ in Eq. (23) under the

following constraints

$$
\begin{aligned}
D = \{\boldsymbol{k} \in \boldsymbol{R^{15}} | &Q_i \in [0,100]\}, i = 1,\dots,8, \\
&R_j \in [0.0001,100], j = 1,2,3, \\
&\alpha_1, \alpha_2 \in [0.01;\ 0.98], \\
&E_c \in [0.01,0.5], \\
&\text{and } r \in [2,10]g.
\end{aligned}
\tag{28}
$$

Here, D denotes the feasible search space. The upper bounds on Q_i, R_j are chosen so that the

penalties on the departures of the states from their desired positions and control utilization is

high. The upper and lower limits of α_1, α_2 suggest that the fractional lengths of the three control

surfaces range from 1% to 98% of the airfoil span length. In contrast to the work proposed in

Singh and McDonough (2014) where α_1 was constrained between 1% and 25% and the lengths

of the second and third control surfaces were fixed, this wider ranges expand the domain of the

search space in the direction of α_1 and α_2 and add another degree of freedom to the design

space. The geometric constraint on the control surface chord fraction E_c is chosen according to

the work presented in Singh et al. (2014). A relationship between the design objectives can be

21

achieved by tuning the individual weights Q_i, R_j, and the control surfaces' widths and lengths.

The design variable r was chosen between 2 and 500 to ensure the estimator is at least two times faster than the fastest closed-loop mode and at most 500 times faster.

To solve this multi-optimization problem, NSGA-II is used. There is no specific guide on how to set up the number of populations and generations for this algorithm. However, according to the MATLAB documentation, the population size can be set in different ways and the default population size is 15 times the number of the design variables n. Also, the maximum number of generations should not be greater than $200xn$. In this study, the population size and the number of iterations is set to $50xn$, where n is the size of the setup variables. The MOP is solved at $V =$ $87.5m/s$, which marks the beginning of flutter and open-loop's instability.

2.8 Results and Discussion

The properties of the Pareto set and Pareto front; sensitives of the dominant poles of the open-loop system, closed-loop system, and estimator to the airspeed; and responses of the controlled, uncontrolled, and observer models at selected objective values are discussed here.

The optimization problem at hand is 15×4. That is, 15 decision variables and 4 objectives. So, it is difficult to depict all the objectives in one graph. Instead, 2D projections from the 4D design space are produced as shown in Figures 3, 4, and 5. The color in these two figures is mapped to the value of the objective $\|B_u K_c\|_F$ with red denotes the highest value, and dark blue denotes the lowest value. It is evident from these figures that there is a competing relationship among the design objectives. For instance, by inspecting the subplots (a) and (b) of Figure 3, we note that at the maximum stability robustness $\lambda_{cmax} = -31.0577$, $\|B_u K_c\|_F$ and $\|L\|_F$ read 2.5633e+06 and 9.6214e+07, respectively. While, at the minimum stability robustness $\lambda_{cmax} =$ -10.1686, $\|B_u K_c\|_F$ and $\|L\|_F$ read 3.0799e+05 and 4.7418e+06, respectively. Another

22

example can be found in Figure 4. We notice that at the best disturbance rejection

$\|GTF(j\omega)\|_{\infty} = 0.0011$, $\|B_u K_c\|_F$ and $\|L\|_F$ read 2.4639e+06 and 9.2596e+ 07, respectively.

While, at the worst gust loads' rejection $\|GTF(j\omega)\|_{\infty} = 0.0057$, $\|B_u K_c\|_F$ and $\|L\|_F$ read

2.3481e + 04 and 5.6637e+ 06, respectively. That is, better disturbance rejection and stability

robustness can be achieved at the high control energy and estimator gain. High estimator gains

may lead to high measurement noise amplifications. A third example is shown in Figure 5 where

there is a conflict between the objective of minimizing the control energy consumption and that

of attenuating sensors' noise amplification. Small values of $\|L\|_F$ and $\|B_u K_c\|_F$ are required to

reduce the impact of measurement noise on the closed-loop performance as indicated by the dark

blue region. On the other side, small energy levels mean bad aerodynamic load repudiation. As a

result, the decision-maker should choose the solution that gives the best compromise between

these objectives.

2.9 Stability Robustness

The profile of the dominant open-loop pole λ_{omax}, closed-loop pole λ_{cmax} at the best

and the worst stability robustness, and the estimator eigenvalue λ_{emax} are shown in Figure 6, 7,

and 8, respectively. Figure 6 shows the open-loop system is sensitive to the airspeed, V (m/s),

and becomes more unstable when V increases. Figure 7 shows the profile of λ_{cmax} at different

degrees of relative stability. As expected, the closed-loop system shows better relative stability at

$\lambda_{cmax} = -31.0577$ than that at $\lambda_{cmax} = -10.1686$. As can be seen from the locations of

max (λ_r) relative to the imaginary axis, border between stability and instability. This stresses the

fact that LQR has very good stability robustness properties (Chen, 2015), which makes it an

attractive choice for the system at hand. That is, regardless of the degree of the relative stability,

the results indicate that the Pareto optimal controls will always stabilize the controlled system at

any airspeed. Meaning the controlled system will never flutter, and the flutter velocity can be boundlessly extended. Moreover, a unique control gain can be designed for the entire flight envelope. In active aeroelastic control, flutter must be placed outside the flight envelope of an aircraft. Typically, a 15% flutter free margin or more is needed beyond the design envelope for both civil and military aircrafts (Carey & Buttrill, 1996). Furthermore, a unique control gain is desired for a designated velocity range of interest because it simplifies the real-time control implementation (Singh et al., 2016). Figure 8 shows the profile of λ_{emax} at different degrees of estimator relative stability. The estimator shows better relative stability at $\lambda_{emax} = -6.5623e + 03$ than that at $\lambda_{emax} = -937.6681$. In general, the estimator dynamics will always be stable regardless the change in the airspeed value.

2.10 Time- Domain Response

For the velocity, V=87.5 m/s (onset of flutter), the closed loop and estimator response is computed when they are excited by a discrete "1-cosine" gust loading (Haghighat et al., 2012). It is clear that the responses at $min(\lambda_{cmax})$ (see Figure 9) $min(\|GTF(j\omega)\|_\infty)$ (see Figure 11) $max(\|B_uK_c\|_F)$ (see Figure 13), and $max(\|L_F\|)$ (see Figure 15) are the best or closest to the knee point. While those at $max(\lambda_{cmax})$ (shown in Figure 10), $max(\|GTF(j\omega)\|_\infty)$ (shown in Figure 12) $min(\|B_uK_c\|_F)$ (shown in Figure 14), and $min(\|L\|_F)$(shown in Figure 16) are the worst or furthest from the knee point. But in all cases, the closed-loop control system can suppress the flutter and stabilize the system and the estimator converges quickly. These responses also confirm the conflicting nature of the design objectives.
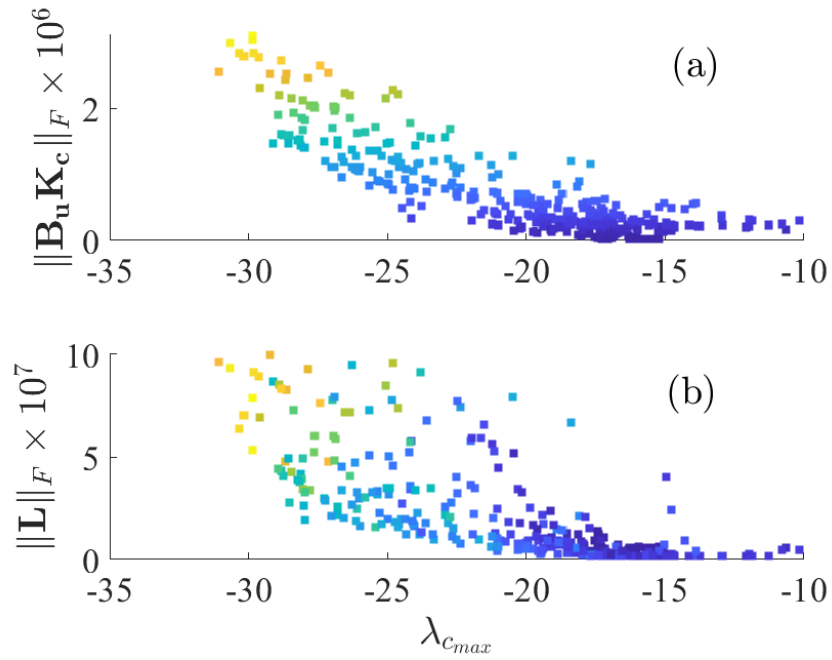
Figure 3: *Projections of the Pareto front. (a)* $\|K_c\|_F$ *versus* $\lambda_{c_{max}}$, *(b)* $\|L\|_F$ *versus* $\lambda_{c_{max}}$. *The color code represents the levels of* $\|B_uKK_c\|_F$ *with red denotes the highest value, and dark blue denotes the lowest value.*

Figure 4: *Projections of the Pareto front. (a) $\|K_c\|_F$ versus $\|GTF(j\omega)\|_\infty$, (b) $\|L\|_F$ versus $\|GTF(j\omega)\|_\infty$. The color code represents the levels of $\|B_uKK_c\|_F$ with red denotes the highest value, and dark blue denotes the lowest value.*

Figure 5: *A 2D projection of the Pareto front. $\|K_c\|_F$ versus $\|L\|_F$. The color code represents the levels of $\|B_uK_c\|_F$ with red denotes the highest value, and dark blue denotes the lowest value.*
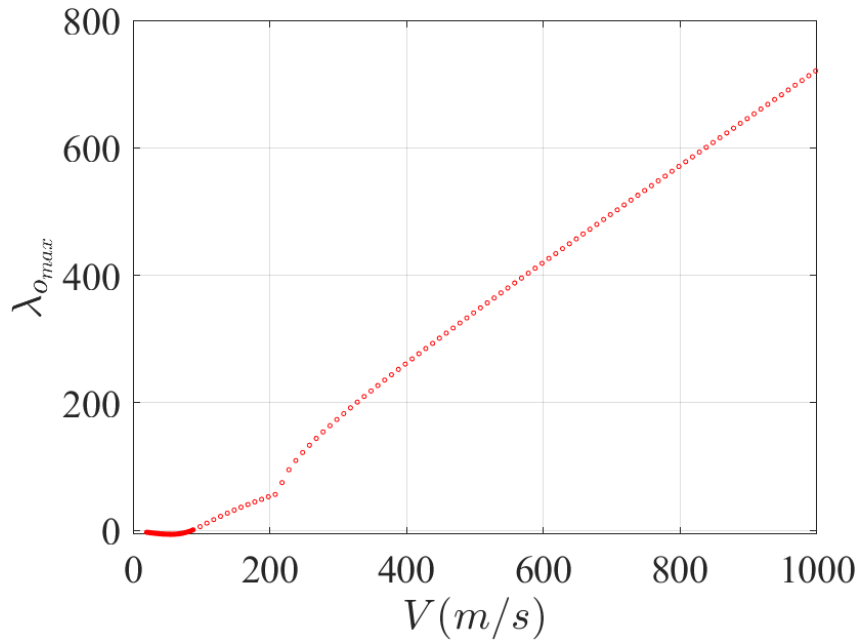
Figure 6: *Profile of the open-loop poles, $\lambda_{o_{max}}$, with change in airspeed*
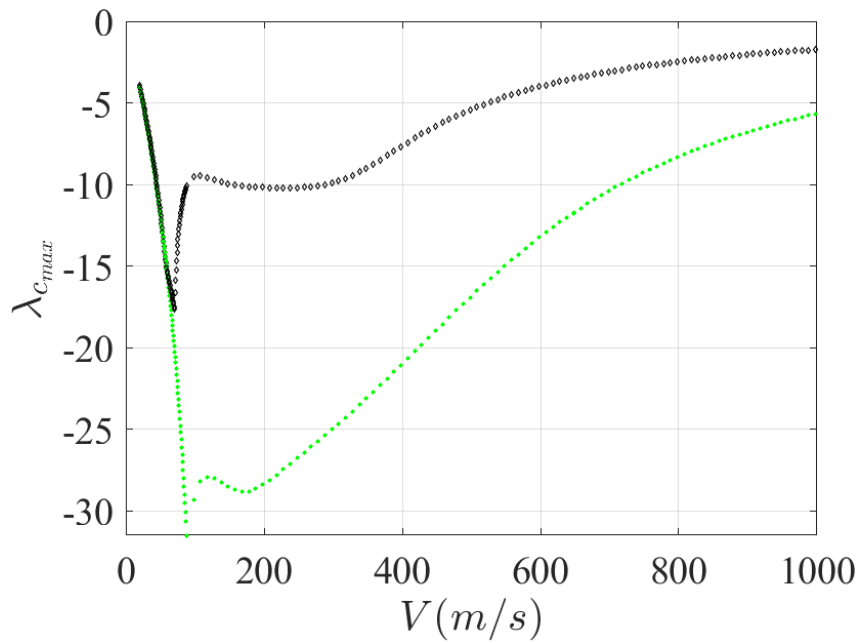
Figure 7: *Profile of the close-loop poles, $\lambda_{c_{max}}$ cmax, with change in airspeed. Green curve with * marker represents $\lambda_{cmax} = -31.0577$. Black curve with diamond marker is the profile of $\lambda_{cmax} = -10.1686$.*

27
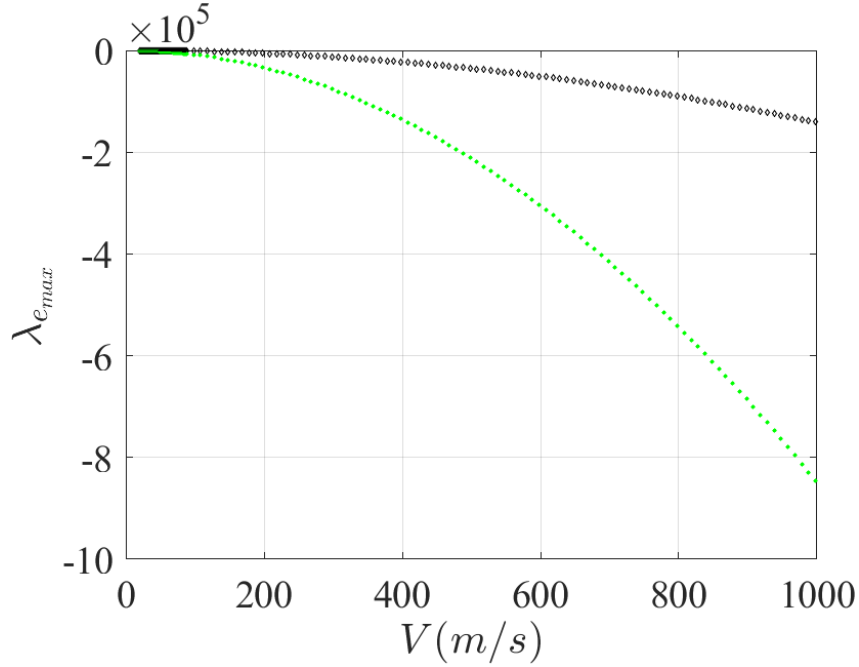
Figure 8: *Profile of the observer poles, λ_{emax}, with change in airspeed. Green curve with * marker represents $\lambda_{emax} = -937.6681$. Black curve with diamond marker is the profile of $\lambda_{emax} = -6.5623 \times 10^3$.*
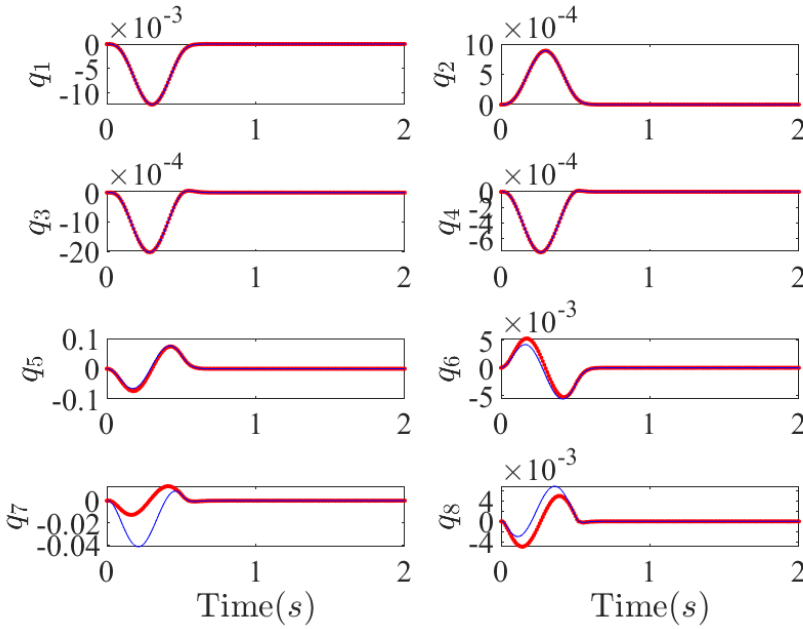
Figure 9: *The response of control surfaces at V=88 m/sec (red solid line: closed-loop response and blue solid line: estimator response at $max (\lambda_{cmax})$.*
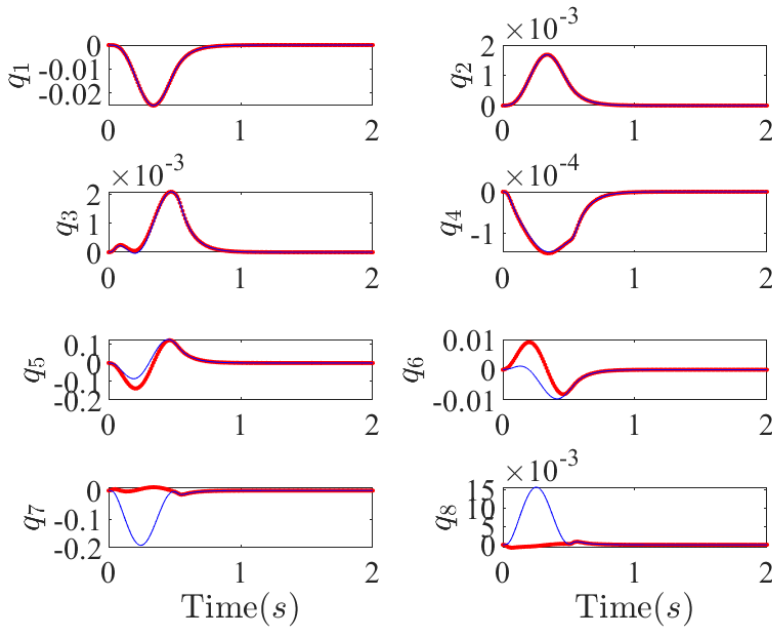
Figure 10: *The response of control surfaces at V=88 m/sec (red solid line: closed-loop response and blue solid line: estimator response at $min(\lambda_{cmax})$.*
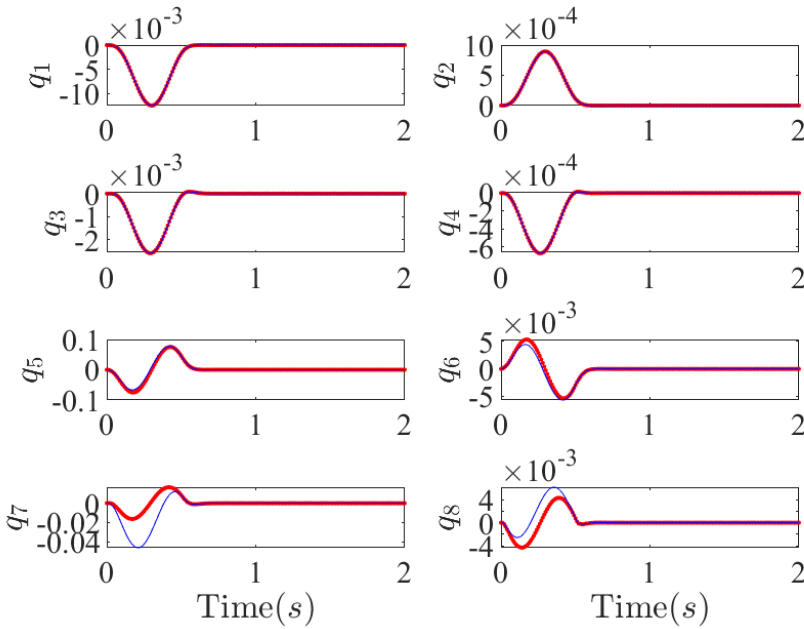
Figure 11: *The response of control surfaces at V=88 m/sec (red solid line: closed-loop response and blue solid line: estimator response at $min(\|GTF(j\omega)\|_\infty)$.*
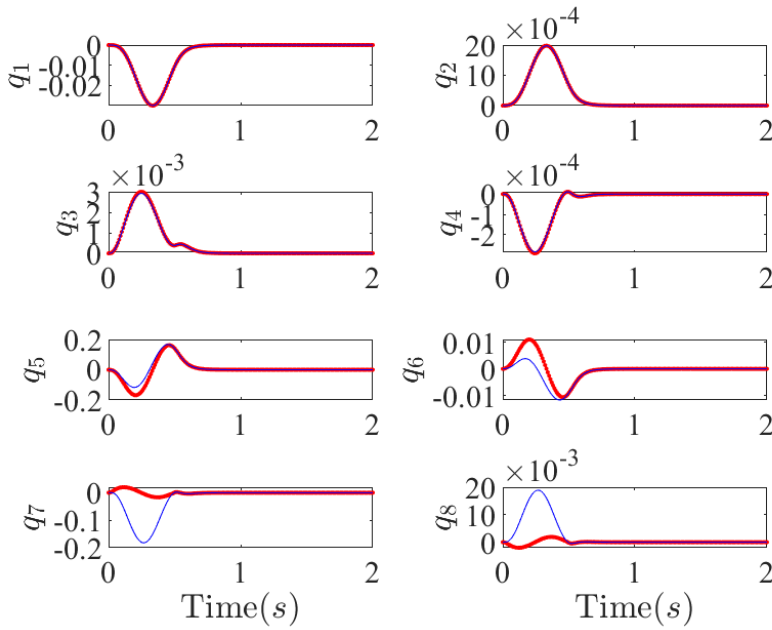
Figure 12: *The response of control surfaces at V=88 m/sec (red solid line: closed-loop response and blue solid line: estimator response at $max(\|GTF(j\omega)\|_\infty)$.*
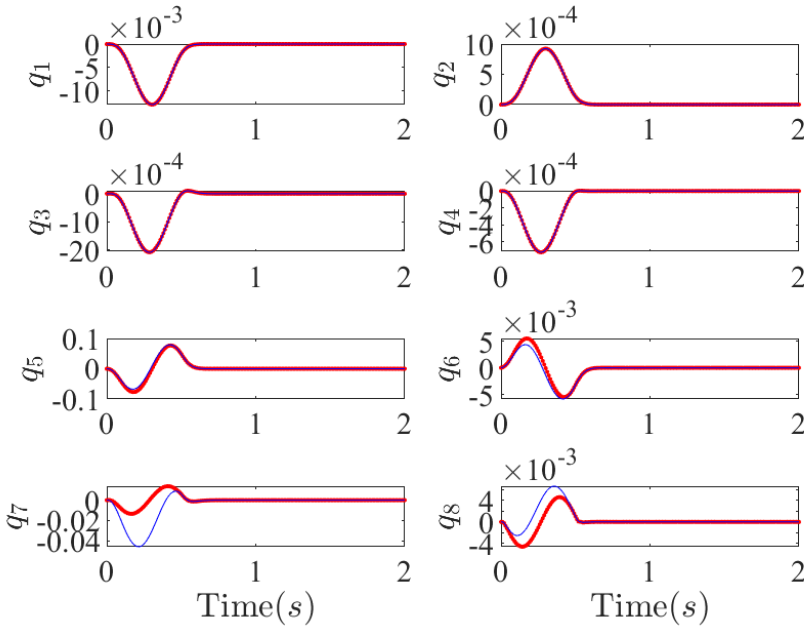
Figure 13: *The response of control surfaces at V=88 m/sec (red solid line: closed-loop response and blue solid line: estimator response at $max(\|B_u K_c\|_F)$.*
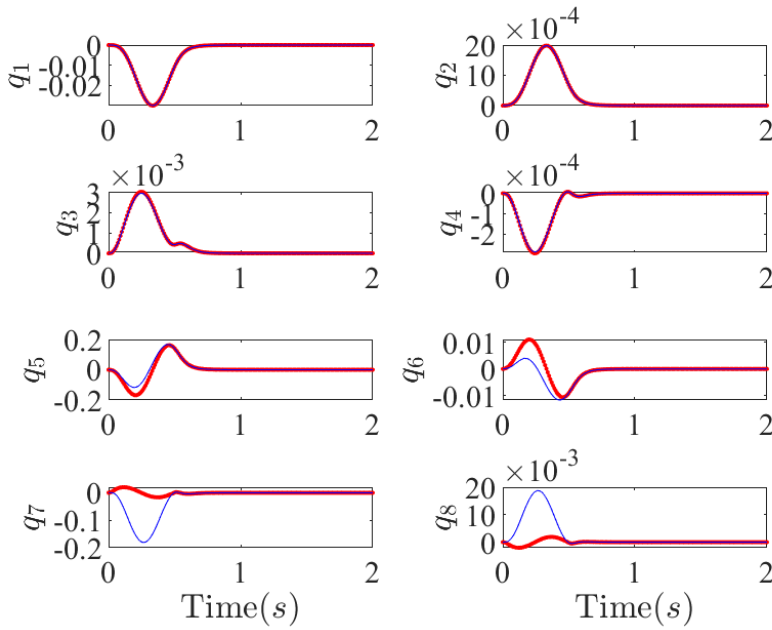
Figure 14: *The response of control surfaces at V=88 m/sec (red solid line: closed-loop response and blue solid line: estimator response at $min(\|BuK_c\|_F)$.*
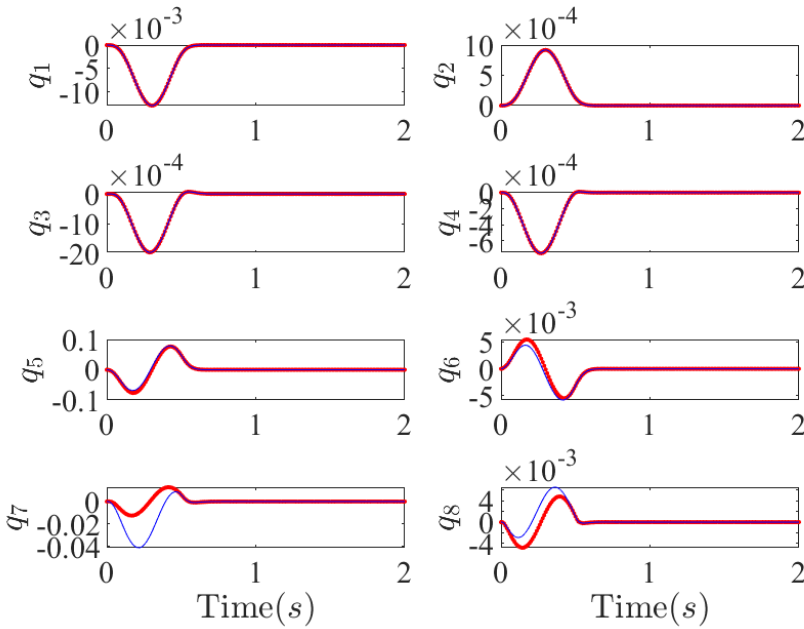
Figure 15: *The response of control surfaces at V=88 m/sec (red solid line: closed-loop response and blue solid line: estimator response at $max(\|L\|_F)$.*
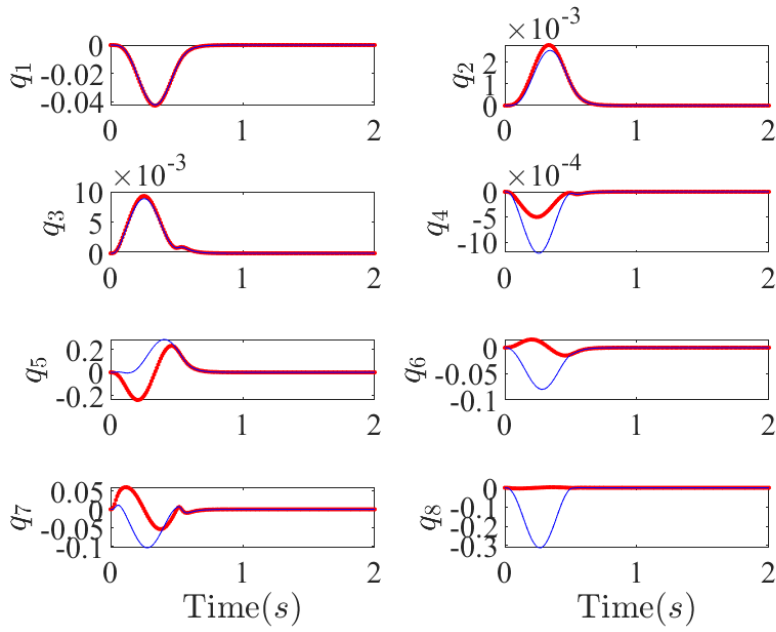
Figure 16: *The response of control surfaces at V=88 m/sec (red solid line: closed-loop response and blue solid line: estimator response at $min(\|L\|_F)$.*

CHAPTER 3: MULTI-OBJECTIVE OPTIMAL DESIGN OF AN ACTIVE AEROELASTIC CASCADE CONTROL SYSTEM FOR AN AIRCRAFT WING WITH A FOUR CONTROL SURFACE

3.1 Introduction

In this chapter, we investigate a multi-objective and multidisciplinary optimal design of a cascade control structure applied to a light-weight wing having four ailerons driven by four DC motors. The cascade control system consists of a primary and secondary control algorithm. The primary control loop uses a full-state feedback controller to compute the desired deflection of each aileron to ensure stability and gust loading alleviation. The output of this controller enters the secondary control loop as a reference signal. The secondary control loop uses a PV controller to drive the actuator to desired levels. The control system design is decoupled into primary and secondary and executed in multi-objective and multidisciplinary settings. The setup gains of the primary and secondary control loops as well as spans and chords of control surfaces are tuned to attain robustness against external upsets, less expenditure of energy, and high-speed ratio of the secondary controller compared to the primary. Under both geometrical and dynamic constraints, the MOP is solved NSGA-II. The optimal solutions are obtained, and a post-processing algorithm is used to help the decision-maker choose a solution for implementation. Robustness of the primary controller against undesired inputs and variation in the free airspeed is investigated.

3.2 Two-Layer Cascade Control System

A cascade control system consists of two feedback controllers, outer (main, master, or primary) and inner (auxiliary, slave, or secondary). Cascade controllers can greatly enhance control performance for disturbances entering the inner loop and is recommended for use when

33

the inner loop is much faster than the outer loop (Corripio, 2000). In this work, the cascade

control system shown in Figure 17 is implemented. The outer control loop uses the dynamics of

the wing and its moveable aerodynamic surfaces to calculate the required control surface rotation

$\boldsymbol{\beta_d}(s)$ to bring the perturbed system states $\boldsymbol{q}(s) = 0$ to their desired equilibrium values

$\boldsymbol{q_d}(s) = 0$. The inner control system takes $\boldsymbol{\beta_d}(s)$ as its reference input and calculates the

required control effort to drive the actuator and bring $\boldsymbol{\beta}(s)$ as close as possible to its desired

level. The primary controller's output serves as the secondary controller's set point. Both control

algorithms should be designed such that they are insensitive to external disturbances

$w_g(s)$ and $D_I(s)$ and measurements noise $(N_O(s)$ and $N_I(s))$. The most important consideration

in designing cascade controllers is the auxiliary loop must be faster than the main loop and the

faster the better (Bolton, 2015). If that is the case, then the secondary controller will take a very

quick corrective action to attenuate the effect of any disturbance that enters the actuators and

prevent its propagation to the primary loop. In fact, if the inner controller is not faster than the

outer one, the cascade design has no advantage, and the overall control system may become

unstable since the slave controller is not acting fast enough to respond to the demands of the

master one. The mathematical model of the wing and its aileron, outer control algorithm,

dynamics of the actuators, and the design of the inner control loop are delineated next.
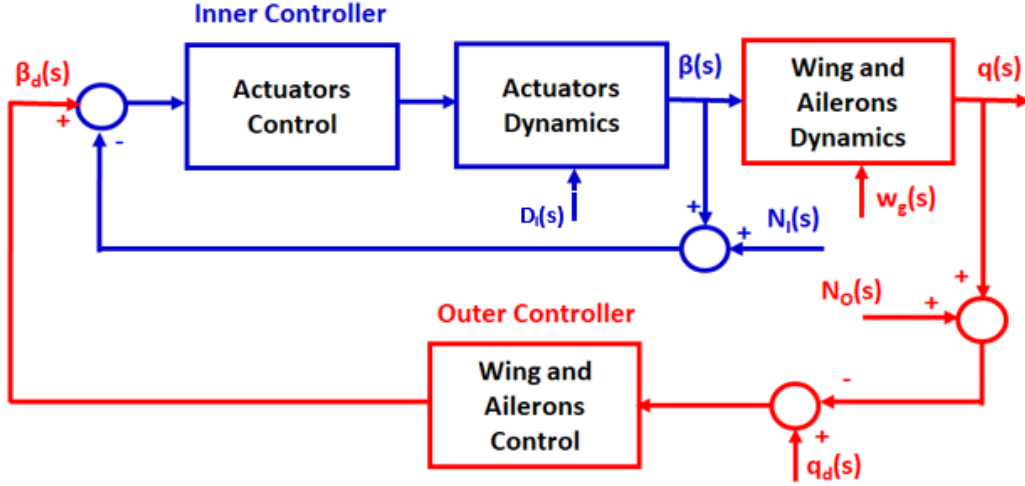
Figure 17: *Cascade control system acting on an aeroelastic structure and actuators.*

3.3 Mathematical Model of an Aircraft's Wing with Multiple Control Surfaces

An aircraft wing (Singh et al., 2014) with four control surfaces is depicted in Figure 18 and its dynamics is described by the following matrix differential equation

$$\boldsymbol{M}\ddot{\boldsymbol{q}}(t) + (\boldsymbol{C} - \rho V\,\boldsymbol{C_a})\dot{\boldsymbol{q}}(t) + (\boldsymbol{K} - \rho V^2\boldsymbol{K_a})\boldsymbol{q}(t) = \boldsymbol{F_c}\boldsymbol{\beta_d}(t) + \boldsymbol{F_g}\boldsymbol{w_g}(t). \qquad (29)$$

Where, **M**, **C**, and **K** denote the structural inertia, damping, and stiffness matrices, respectively. While, $\boldsymbol{C_a}$ and $\boldsymbol{K_a}$ are respectively the aerodynamic damping and stiffness matrices. The vector $\boldsymbol{q}(t) = [q_1(t), q_2(t), q_3(t), q_4(t)]^T$ represents the generalization coordinates; $\boldsymbol{\beta_d}(t) = [\beta_1(t), \beta_2(t), \beta_3(t)]^T$ is the vector of the control surfaces' deflections; and $\boldsymbol{F_c}$ describes the influence of the control vector on the system dynamics. The vector $\boldsymbol{w_g}(t)$ models the external gust loads and $\boldsymbol{F_g}$ represents the influence of these loads on the model. The variable V is the airspeed (m/s) and ρ is the air density (kg/m^3). The reader can refer to Appendix C for more details about the model and the numerical values used in the computer simulation.

The bending deformation (transverse deflection) z and rotation θ at any point $(x; y)$ on the wing are related to the generalized coordinates and the wing's dimensions by the following equations:

$$z = y^2 q_1 + y^3 q_2 + y(x - x_f)q_3 + y^2(x - x_f)q_4 \qquad (30)$$

$$\theta = y q_3 + y^2 q_4 \qquad (31)$$

where, x_f is the flexural axis location aft of leading edge. The parameters s_1, s_2, s_3, and s_4 decide the span lengths and locations of the control surfaces, while E_c denotes the fraction chord of each aileron. These variables are of special interest since they dictate the sizing and location of the flabs but also the amount of control energy required to drive them and ability of the structure to reject aerodynamic loads. The system in Eq. (29) can be re-written as

$$\ddot{q}(t) = M^{-1}(F_c \beta_d(t) + F_g w_g(t) - (C - \rho V C_a)\dot{q}(t) - (K - \rho V^2 K_a)q(t), \qquad (32)$$

which can be represented by the following state-space model

$$\dot{x}(t) = A x(t) + B_u \beta_d(t) + B_g w_g(t). \qquad (33)$$

The output equation is given by

$$y(t) = C_o x(t) \qquad (34)$$

The state vector is defined as

$$x(t) = [q_1(t), q_2(t), \ q_3(t), q_4(t), \dot{q}_1(t), \dot{q}_2(t), \dot{q}_3(t), \dot{q}_4(t)]^T \qquad (35)$$

The system matrices A, B_u, B_g, and C_o are given by

$$A = \begin{bmatrix} 0_{4\times4} & I_{4\times4} \\ -M^{-1}(K - \rho V^2 K_a) & -M^{-1}(C - \rho V C_a) \end{bmatrix} \qquad (36)$$

$$B_u = \begin{bmatrix} 0_{4\times4} \\ M^{-1}F_g \end{bmatrix} \qquad (37)$$

$$B_g = \begin{bmatrix} 0_{4 \times 4} \\ M^{-1}F_g \end{bmatrix} \qquad (38)$$

$$C_o = [I_{4 \times 4} \quad 0_{4 \times 4}]. \qquad (39)$$

Where, **I** and **0** denote the identity and zero matrices, respectively. The dynamics of the system is

now in the standard state-space form and a control system can be designed.
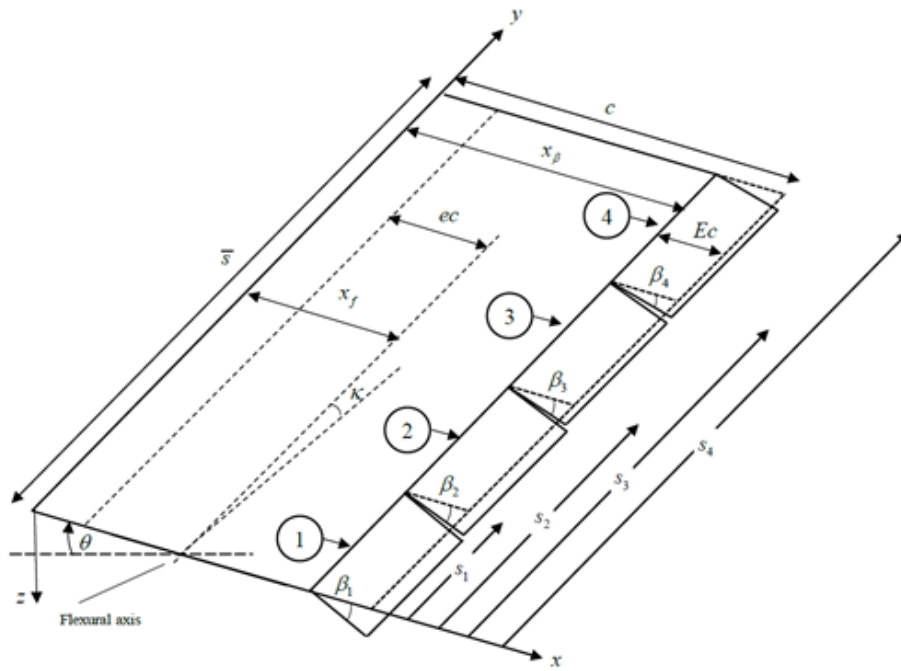
Figure 18: *Flexible aircraft wing model with four control surfaces (Singh et al., 2014).*

3.4 Primary Control System

A MIMO full-state feedback law for the state-space system given in Eq. (33) can be

written as

$$\beta_d(t) = -K_c x(t), \qquad (40)$$

where, $\boldsymbol{K_C} \in \mathbb{R}^{4\times8}$ is the state feedback gain matrix. Substituting Eq. (40) into Eq. (33), the closed-loop dynamics is given by

$$\dot{\boldsymbol{x}}(t) = (\boldsymbol{A} - \boldsymbol{B_u}\boldsymbol{K_C})\boldsymbol{x}(t) + \boldsymbol{B_g}\boldsymbol{w_g}(t). \qquad (41)$$

Taking the Laplace of Eq. (41), we obtain

$$(s\boldsymbol{I} - \boldsymbol{A} + \boldsymbol{B_u}\boldsymbol{K_C})\boldsymbol{X}(s) = \boldsymbol{B_g}\boldsymbol{W_g}(s), \qquad (42)$$

where, $\boldsymbol{X}(s)$ and $\boldsymbol{W_g}(s)$ are the Laplace transforms of $\boldsymbol{x}(t)$ and $\boldsymbol{w_g}(t)$, respectively. Using this equation and Eq. (34), the transfer function matrix $\boldsymbol{GTF}(s)$ from the gust loads to the system's outputs is provided by

$$\boldsymbol{GTF}(s) = \frac{Y(s)}{W_g(s)} = \boldsymbol{C_o}(s\boldsymbol{I} - \boldsymbol{A} + \boldsymbol{B_u}\boldsymbol{K_C})^{-1}\boldsymbol{B_g}. \qquad (43)$$

Here, $\boldsymbol{Y}(s)$ denotes the Laplace transform of $\boldsymbol{y}(t)$. This transfer function matrix is very crucial in the design of an aircraft's wing since one of the design requirements is to alleviate the impacts of extreme aerodynamic loads on the system performance. It is obvious that by increasing the values of the elements of the feedback gain matrix $\boldsymbol{K_C}$, the gust loads' can be attenuated. However, this conflicts with the requirement of minimizing the control energy needed to stabilize the system and suppress flutter. The state feedback gain matrix $\boldsymbol{K_C}$ can be designed in different ways. One of the popular methods in classical optimal control is the Linear Quadratic Regulator (LQR). The optimal state feedback control gain matrix $\boldsymbol{K_C}$ can be obtained by minimizing the following performance index:

$$J = \int_0^\infty [\boldsymbol{x}^T\boldsymbol{Q}\boldsymbol{x}(t) + \boldsymbol{u}^T(t)\boldsymbol{R}\boldsymbol{u}(t)]\, dt, \qquad (44)$$

where $\boldsymbol{Q} = \boldsymbol{Q}^T$ is a positive semidefinite matrix that penalizes the departure of system states from their equilibrium points, and $\boldsymbol{R} = \boldsymbol{R}^T$ is a positive definite matrix that penalizes the control input. Using Lagrange multiplier-based optimization method, the optimal $\boldsymbol{K_C}$ is given by

38

$$K_C = R^{-1}B_u^T P. \tag{45}$$

The matrix $P \in \mathbb{R}^{8\times3}$ can be calculated by solving the following Algebraic Riccati Equation (ARE):

$$A^T P + PA - Q - PBR^{-1}B_u^T P = 0 \tag{46}$$

By examining Eqs. (45) and (46), we can notice that the weighting matrices **Q** and **R** play an important role in the LQR optimization process. That is, the elements of the **Q** and **R** matrices affect greatly the performance of a closed-loop system. Thus, the most important step in the design of an optimal controller using LQR is the choice of **Q** and **R** matrices. Conventionally, these matrices are elected based on the designer's experience and adjusted iteratively to obtain the desired performance. Arbitrary selection of **Q** and **R** will result in a certain system response which is not optimal in true sense. Many efforts have been directed toward developing systematic methods for selecting the weighting matrices. For instance, Bryson presented an approach for choosing the starting values of **Q** and **R** matrices, but this method only suggests the initial values and later the coefficients are to be tuned iteratively for optimal performance (Bryson, 2018). Hence, an optimization algorithm is needed to tune the elements of these matrices such that the desired response is achieved. Analytical way of selecting the **Q** and **R** matrices for a second order crane system was developed in Oral et al. (2010). Another analytical method of calculating the **Q** and **R** matrices for a third order system represented in the control canonical form was proposed in El Hajjaji and Ouladsine (2001). Developing an analytical technique to find **Q** and **R** for high order systems such as the system at hand is very tedious if it is not possible because of the dimension of the system. Therefore, we suggest a numerical approach through using an optimization algorithm to tune these matrices such that the design goals are optimized simultaneously.

3.5 Actuator Dynamics

Conventional hydraulic actuators (HAs) have been widely used in aircraft systems such as Airbus A380 and Gulfstream G65026. However, they require high maintenance, and their performance is sensitive to both pressure and temperature which in turn leads to high operating costs and low efficiency. Recently, there has been a tendency in the aerospace domain towards increasing the exploitation of electrical-mechanical actuators (EMAs) in aircraft applications. These actuators have been recently introduced in large commercial aircrafts such as Airbus A380 and Boeing 787. Compared to HAs, EMAs have higher energy efficiency; better dynamic characteristics; smaller weights, better safety, reliability, and diagnostic features because they do not use any poisonous and flammable hydraulic fluids; less power transmission complexity; and less maintenance cost since they do not experience hydraulic leaks. There are two common types of EMAs: linear and rotary. In the case of linear EMAs, the rotational motion of the motor is converted into linear by a ball-screw mechanism. While in the case of rotary EMAs, the motor output shaft is connected to a gearbox to increase its torque and reduce its angular speed. Then, the output shaft of the gearbox is connected to the moveable aerodynamic surface either directly to the hinge line or by a connecting rod assembly (Habibi, Jeff, and Greg, 2008), (Qiao et al., 2018). Here we choose a linear EMA driven by a power amplifier and its output shaft is connected to a ball-screw mechanism which drives a slider-crank mechanism converting the linear movement of the ball-screw mechanism into a control surface deflection as shown in Figure 19.
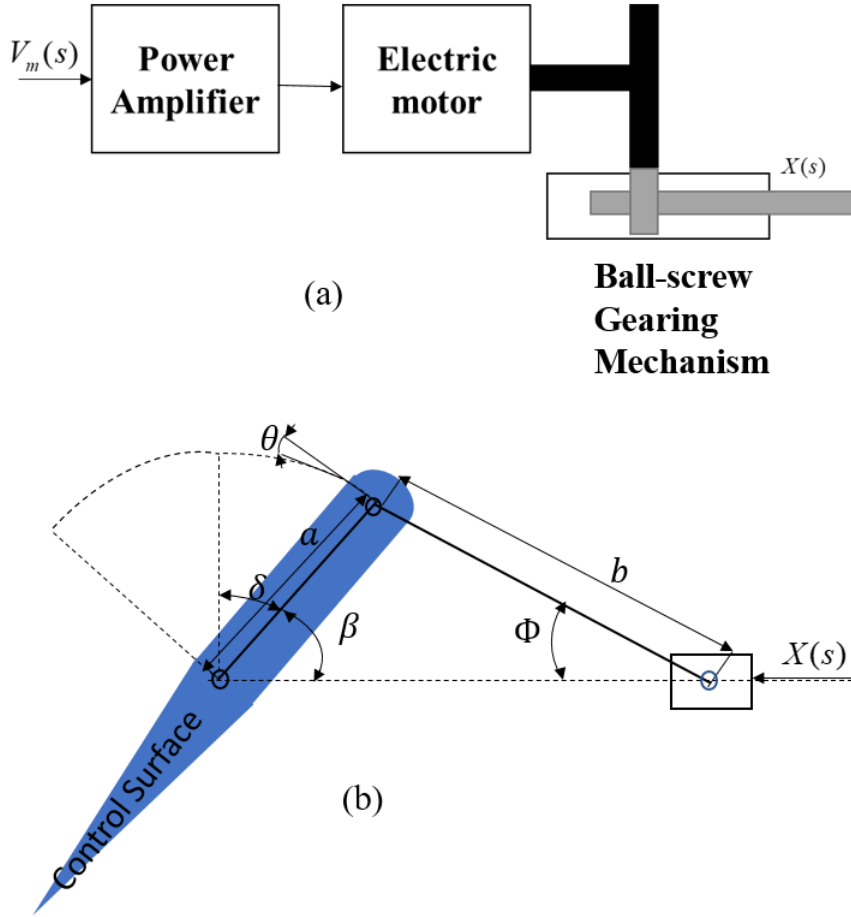
Figure 19: *(a) EMA components (Habibi et al., 2008), and (b) slider-Crank Mechanism (Zhang and Zhou, 2017).*

The dynamics of the amplifier, electric motor, and gearbox assuming it does not have a backlash

is given by

$$\frac{X(s)}{V_m(s)} = \frac{K_a}{s(\tau s+1)},$$

(47)

where, $V_m(s)$ is the input voltage, $X(s)$ is the linear displacement of the gearbox. Following the

work presented in Habibi et al. (2008), the DC gain of the motor K_a and time constant τ are set

to 0.0452 and 0.0026, respectively.

The deflection of the aileron can be calculated from the kinematic equations of the slider-

crank mechanism and it is given by:

$$\beta = \cos^{-1}\left[\frac{(1+n-X/a)^2 - n^2 + 1}{2(1+n-X/a)}\right].$$ (48)

Where, $n = b/a$. Following the work proposed in (Zhang and Zhou, 2017), the length of crank

a is set to 100 mm; and the length of linkage b is set to 170 mm. On the other side, the required

linear movement of the ball-screw mechanism X to achieve this value of β can be calculated as

follows

$$X = a\left[n\left(1 - \sqrt{1 - \frac{\sin^2(\beta)}{n^2}}\right) + 1 - \cos(\beta)\right].$$ (49)

Since we are dealing with a wing having four control surfaces, four EMAs and slider-crank

mechanisms are required. Furthermore, the dynamics of the slider-crank mechanisms is not

included in the simulation and will consider in future studies. That is, only the above kinematic

equations are used to convert X into β and vice versa. Our focus is on decoupling the control

system design into a primary and secondary loop by considering the dynamics of the wing and

the EMA. More details about the motor model and the kinematic equations of the slider-crank

mechanism can be found in Appendix B.

3.6 Secondary Control Loop

The dynamics of the actuators greatly affect the performance of the aeroelastic structure.

Assuming that all the flaps are driven by identical EMAs and their dynamics are given in Eq.

(47), the dynamic of the actuators can be described by the following differential equation

$$\tau\ddot{X}(t) + \dot{X}(t) = K_a(V_m(t) + D_I(t)).$$ (50)

Here, $D_I(s)$ denotes external disturbances affecting the actuators as shown in Figure 17.

Inspecting the dynamics of the system, we notice the system already has integrator dynamics. As

a result, a simple PV (Proportional-Velocity controller is enough to stabilize the system and

provide a good tracking. The PV control law is given by

$$V_m(t) = k_p\big(X_d(t) - X(t)\big) - k_v \dot{X}(t), \tag{51}$$

Where k_p and k_v are respectively the proportional and velocity gains. Substituting Eq. (51) into

Eq. (50), applying Laplace transformation, and simplifying, we get

$$X_j(s) = \frac{K_a}{\tau s^2 + \big(1 + K_a k_{v_j}\big)s + K_a k_{p_j}}\Big[k_{p_j} X_d(s) + D_{I_j}(s)\Big]. \tag{52}$$

Using the superposition principle and setting $X_d = 0$, the disturbance sensitivity function is

given by

$$DSF_j = \frac{X_j(s)}{D_{I_j}(s)} = \frac{K_a}{\tau s^2 + \big(1 + K_a k_{v_j}\big)s + K_a k_{p_j}}. \tag{53}$$

The closed-loop characteristic equation read

$$CE_j = \tau s^2 + \big(1 + K_a k_{v_j}\big)s + K_a k_{p_j} \tag{54}$$

Where $j = 1, 2, \dots, 4$. These equations are very useful in the design of the control system. One

of the design goals in this work is to attenuate the impacts of $D_{I_j}(s)$ and prevent them from

propagating to the outer loop. To this end, Eq. (53) can be used to quantify these impacts. Also,

the speed of responses of the inner control systems should be at least two times faster than that of

the outer control loop. The speed of response of any system is a function of its dominant closed

loop poles which can be found from Eq. (54). Furthermore, the control energy expenditure of the

actuators can be quantified by using the Frobenius norm of their control parameters as follows

$$E_J = \sqrt{\left|k_{p_j}\right|^2 + \left|k_{v_j}\right|^2} \tag{55}$$

Having all the objectives defined and all the tuning parameters specified, the multi-

objective optimization can be readily formulated.

3.7 Multi-Objective Optimal Design

The design variables of the primary and secondary controllers as well as the geometrical parameters of the control surfaces are tuned by the NSGA-II. The decision vector is given by,

$$\boldsymbol{k} = \left[Q_1, \ldots, Q_8, \; R_1, \ldots, \; R_4, \; \alpha_1, \ldots, \alpha_3, \; E_c, \; k_{p_1}, \ldots, k_{p_4}, k_{v_1}, \ldots, k_{v_4} \right]. \tag{60}$$

The parameters $Q_1, \ldots, Q_8$ and $R_1, \ldots, R_4$ are the diagonal elements of $\mathbf{Q}$ and $\mathbf{R}$, respectively. These design variables are employed to indirectly tune $\boldsymbol{K}_C$. The sizes and locations of the control surfaces are tuned by and adjusting their span-wise ($\alpha_1, \ldots, \alpha_3$) and chord lengths($E_c$). While, $k_{p_1}, \ldots, k_{p_m}, k_{v_1}, \ldots, k_{v_m}$ are the setup gains of the auxiliary control algorithms. The constraints on the design variables are defined as follows:

$$D = \left\{ \boldsymbol{k} \in \mathbb{R}^{24} \; \middle| \; \begin{array}{c} Q_1, \ldots, Q_4 \in [0, 100] \\ R_1, \ldots, R_m \in [0.00001, 100] \\ a_1, \ldots, a_{m-1} \in [0.01, 0.97] \\ E_c \in [0.01, 0.25] \\ k_{p_1}, \ldots, k_{p_m} \in [10 \times 10^3, 30 \times 10^6] \\ k_{v_1}, \ldots, k_{v_m} \in [100, 300] \end{array} \right\} \tag{61}$$

The upper and lower limits of $Q_1, \ldots, Q_8$ and $R_1, \ldots, R_4$ are chosen so that the penalties on the departures of the states from their equilibrium values and control energy expenditure change widely from low to high values. This choice expands the search space of these variables and allows the optimization algorithm to find all the optimal trade-offs solution within this space. The ranges of $\alpha_1, \ldots, \alpha_3$ allows the span-wise length of the four ailerons to change from 0.01 to 0.97 of the wingspan lengths. It is worth noting the length of the fourth control surface is given by: $[1 - (\alpha_1, \; \alpha_2, \alpha_3)] \times \bar{s}$. So, only three design parameters are needed to tune the span-wise lengths. Following the work presented in 12, E_{c_j} is chosen to be between 0.01 and 0.25. The ranges of the inner control gains are chosen according to stability constraint required by Eq. (54)

and to guarantee that the secondary control loop is faster than the primary one. These setup gains are optimally tuned to simultaneously achieve the following cost functions:

$$\min_{k \in D}\{-r, D_{av}, E_{av}\} \qquad (62)$$

The objective r quantifies speed ratio of the secondary controlled systems versus the primary feedback control loop, and it is given by

$$r = \frac{\lambda_{S_{Mx}}}{\lambda_{P_{Mi}}}, \qquad (63)$$

where $\lambda_{S_{Mx}}$ is the dominant closed-loop eigenvalue from the four secondary controlled loops and $\lambda_{P_{Mi}}$ is the fastest mode of the primary control structure. Mathematically, $\lambda_{S_{Mx}}$ and $\lambda_{P_{Mi}}$ read

$$\lambda_{S_{Mx}} = max\left[max\left(real\left(eig(CE_J)\right)\right)\right]. \qquad (64)$$

$$\lambda_{P_{Mi}} = max\left[max\left(real(eig(A - BK_C))\right)\right]. \qquad (65)$$

The function eig finds the eigenvalues of the system, $real$ function returns only the real parts of these eigenvalues, max returns the dominant pole, and min returns the smallest value of its input, which is in our case the fastest pole. To ensure that the inner control system has a faster reaction time than the outer one, the following constraint was applied to the objective space

$$r > 2. \qquad (66)$$

This could be roughly interpreted as the secondary reaching its steady state in one-half the time of the primary after an open loop step change in the manipulated variable. This constraint also ensures that closed-loop eigenvalues of the inner closed-loop system are separated from those of the outer one. The attenuation of external disturbances affecting both control loops can be quantified by

$$D_{av} = \frac{1}{2}\left[\left\|GTF(i\omega_l)\right\|_\infty + max_j(\left\|DSF_j(i\omega_2)\right\|_\infty)\right], \qquad (67)$$

where $GTF(j\omega)$ is the ∞ - *norm* of transfer function defined in Eq. (43) and returns the maximum value among the ∞ - *norm* of DSF_j given in Eq. (53). It should be noted that small values of these functions indicate better disturbance rejection. The variable $\omega_1 \in [0, 100]$ as suggested in Singh et al. (2014). The values of ω_2 and $\omega_3 \in [0, 2]$ as proposed in Sardahi and Boker (2018). The third objective in Eq. 62 defines the average control energy of the slave controllers

$$E_{av} = mean[E_j], j = 1, ..., 4. \tag{68}$$

The operator *mean* returns the average value of the Frobenius norms defined in Eq. (55).

To solve this multi-objective optimization problem with the objective and decision spaces defined respectively in Eq. (62) and Eq. (60) under the constraints of Eq. (61) and Eq. (66), the non-dominated sorting genetic algorithm (NSGA-II) is used. There is no specific guide on how to set up the number of populations and generations for this algorithm. However, according to the MATLAB documentation, the population size can be set in different ways and the default population size is 15 times the number of the design variables $nvar$. Also, the maximum number of generations should not be greater than $200 \times nvar$. In this study, the population size and maximum number of iterations are set to $50 \times nvar$, where $nvar$ is equal to 24.

3.8 Numerical Results

Properties of the Pareto front and Pareto set, responses of the primary and secondary controlled systems to external disturbances and measurement noise, and robustness of the primary controller to air stream velocity V at $\lambda_{PM_x} = max\left[real\big(eig(A - BK_C)\big)\right]$ are discussed here.

3.9 Properties of Pareto Cascade Optimal Controls

The Pareto front and six different projections from the Pareto set are shown in Figure 20-26. The size of the Pareto front is 720×3 and that of the Pareto set is 720×24. That is, there are 720 optimal and compromise solutions to choose from. Each point on the front expresses a different degree of trade-off among the design objectives. The Pareto front shows a conflicting relationship between $\boldsymbol{E}_{av}$ and $\boldsymbol{D}_{av}$. For instance, at $\boldsymbol{E}_{av} = 8.3637 \times 10^5$, $\boldsymbol{D}_{av}$ reads 1.0970×10^{-3}; while at $\boldsymbol{E}_{av} = 9.5276 \times 10^6$, $\boldsymbol{D}_{av}$ is 0.728×10^{-3}. Despite this non-agreement relationship between the two objectives, the values of $\boldsymbol{D}_{av}$ show the proposed cascade control system has a very good disturbance capability. The Pareto front also shows the speed ratio between the inner and outer is greater than 2, which is one of the requirements in the design of cascade control system. We also notice that when r is 3.0099, $\boldsymbol{E}_{av}$ is equal to 8.3637×10^5; while at the maximum value of the speed ratio ($r = 74.9257$), $\boldsymbol{E}_{av}$ reads 5.8055×10^6. Between these two points, we can find large values of r associated with small energy and vice versa. For example, at $r = 6.0310$, $\boldsymbol{E}_{av} = 3.6943 \times 10^6$; while at $r = 24.8903$, $\boldsymbol{E}_{av} = 2.5462 \times 10^6$. However, by inspecting the Pareto front we notice that $\boldsymbol{D}_{av}$ at $r = 6.0310$ and $r = 24.8903$ reads 0.6068×10^{-3} and 1.2646×10^{-3}, respectively. Meaning, even though it is attractive to ensure that the speed ratio is high, and the control energy is small, the disturbance attenuation should be also high especially for the system at hand which experiences unavoidable aerodynamic gust loads. The optimization algorithm returns 720 optimal implementations of the cascade control with different control gains and aileron sizes. So, it is up to the decision-maker to choose which point to implement. However, some post-processing algorithm such as that reported in Sardahi and Sun (2017) can be used to help the decision-maker. The algorithm starts by finding the ideal point ($\boldsymbol{P}_I$ as shown in Figure 20) of the

Pareto front. This point is made of the minimum values of all the objectives and so it is not the Pareto front. It is worth noting this point cannot be found by any optimization algorithm due to the competing relationships among the design objectives. Then, the Euclidean distance between each point on the Pareto front and P_I is calculated. After that, the Euclidean distance values are sorted in an ascending order with the first point labeled P_N and the last point labeled P_F. So, implementing P_N can be appealing to the designer since it is the closet point to P_I. P_F is one of the optimal solutions, but it can be less catchy to the decision-maker because it is the furthest point from P_I. Between P_N and P_F there are many other optimal options. These two points were also added to the six projections of the Pareto set as shown in Figure 21-26. The color codes are explained in the captions of these figures. Figure 21 shows that the optimal ranges of $\alpha_1, \alpha_2, \alpha_3$, are [0.0175, 0.0933], [0.0300, 0.1825], and [0.7277, 0.8611], respectively. As a result, the span length of the fourth control is between 0.0102 and 0.1362 of the wingspans. That is, to achieve the selected design objectives simultaneously, the optimization algorithm suggests keeping the span-wise lengths of the two middle ailerons greater than those attached to left and right edge of the wing. The color code in this figure is mapped to the value of E_C and its optimal is between 0.0144 and 0.2473. At P_N, $r = 5.2498$, $D_{av} = 0.909 \times 10^{-3}$, $E_{av} = 1.4117 \times 10^6$ and the design parameters are given by

$$Q_{1\ldots8} = [90.5589, 73.4348, 10.8965, 43.1048, 0.3958, 25.1081, 0.0141, 1.2945] \quad (69)$$

$$R_{1\ldots4} = [63.9256, 75.1654, 61.0558, 85.0132] \quad (70)$$

$$\alpha_{1\ldots3} = [0.0640, 0.1005, 0.7501] \quad (71)$$

$$E_c = 0.2092 \quad (72)$$

$$k_{P1\ldots4} = [1.5884, 2.9971, 3.1380, 3.2453] \times 10^6 \quad (73)$$

$$k_{v1\ldots4} = [609.4665, 731.7387, 904.4938, 890.7366] \quad (74)$$

48

While at $\boldsymbol{P_F}, r = 71.6299, \boldsymbol{D}_{av} = 1.11 \times 10^{-3}, \boldsymbol{E}_{av} = 8.6510 \times 10^6$ and the design

parameters are given by

$$Q_{1\ldots8} = [93.5302, 65.2186, 50.9763, 38.9561, 0.1466, 11.0741, 0.0055, 0.1585] \quad (75)$$

$$R1\ldots4 \; R_{1\ldots4} = [47.6938, 70.2664, 85.8683, 88.0736] \quad (76)$$

$$\alpha_{1\ldots3} = [0.0648, 0.0822, 0.8060] \quad (77)$$

$$E_c = 0.2332 \quad (78)$$

$$k_{P1\ldots4} = [10.271, 10.270, 28.636, 12.901] \times 10^6 \quad (79)$$

$$k_{v1\ldots4} = [1.4063, 1.3806, 1.4644, 1.4735] \times 10^3 \quad (80)$$

It can be noticed that a cascade controller designed at $\boldsymbol{P_N}$ will have less energy consumption and

better disturbance rejection than that designed at $\boldsymbol{P_F}$. On the other side, the speed ratio of the

inner control algorithm to the outer one is better if the implementation is done at $\boldsymbol{P_F}$. When r is

large, the inner closed-loop system will attenuate $\boldsymbol{D_I}$ (see Figure 17) very quickly before it

propagates to the outer one. The closed-loop response of the inner and outer control algorithm is

discussed next.

3.10 Effect of External Disturbances

The response of the inner and outer controlled systems is simulated assuming zero initial

conditions and under the excitation of a discrete "1-cosine" gust loading disturbing the primary

loop and a sinusoidal internal disturbance given by

$$w_{g_j}(t) = \frac{\bar{w}_g}{2}\left(1 - \cos\frac{2\pi t}{L_g}\right) for \; 0 < t > \boldsymbol{L_g}. \quad (78)$$

$$D_{J_j}(t) = A\sin(\omega t) \quad (79)$$

Here, $\bar{w}_g$ is the maximum gust velocity, and $\boldsymbol{L_g}$ is the total length of gust bump. Following the

work proposed in Haghighat et al. (2012), we set $\boldsymbol{L_g}$ to 0.5s. Different from this work, we set $\bar{w}_g$

to 10×4.575 m/s instead of 4.575 m/s to show the ability of both control layers to deal with this upset. The amplitude of A and ω are set to 1 and 2, respectively. The index $j = 1, \ldots, 4$ since we have four ailerons and actuators. Using Eq. (30), the deflection of the wing in the z-direction is calculated at the following points

$$(x, y) = [(-0.3, 1)\ (-0.2, 4)\ (0.1, 5)\ (0.4, 2)] \tag{80}$$

The time response of $z_1(t)$ to $z_4(t)$ at either $\boldsymbol{P_N}$, and $\boldsymbol{P_F}$ (Figures 27 and 28) show the outer control algorithm can successfully stabilize regardless of the aerodynamic loads. The tracking behaviors of the inner loop at these two design options are shown in Figures 29 and 30. Since the dynamics of the secondary controlled system was made faster than that of the primary closed-loop system, the tracking error between $\beta(t)$ and $\beta_d(t)$ is very small. Tracking absolute errors are tabulated in Table 1. The table shows the tracking errors at $\boldsymbol{P_F}$ are smaller than those at $\boldsymbol{P_N}$ which is due to the high speed of ratio at $\boldsymbol{P_F}$ compared to that at $\boldsymbol{P_N}$. The profiles of the input voltages shown in Figures 31 and 32 show similar behavior because the acting external disturbances are the same and the dimensions of the ailerons at these two points are also very close from each other.

Table 1: *Inner controller racking absolute errors at PN, and PF*

	$\int_0^t \left\| \beta_{d_1} - \beta_1 \right\| d\tau$	$\int_0^t \left\| \beta_{d_2} - \beta_2 \right\| d\tau$	$\int_0^t \left\| \beta_{d_3} - \beta_3 \right\| d\tau$	$\int_0^t \left\| \beta_{d_4} - \beta_4 \right\| d\tau$
P_N	0.1028×10^{-5}	0.1028×10^{-5}	0.6568×10^{-5}	0.3698×10^{-5}
P_F	0.0311×10^{-5}	0.0311×10^{-5}	0.3239×10^{-5}	0.1997×10^{-5}

3.11 Effect of Air Stream Velocity

It is very important to ensure the closed-loop outer system is stable regardless of the variation in V. At $\lambda_{P_{Mx}}$, the relative stability of the primary controlled system is the lowest. Among the closed-loop eigenvalues, this pole is the closet one to the boundary between stability

and instability. So, if the closed-loop system stays stable at this value as V varies, the other optimal options will also guarantee stability. To this end, the profile of $\lambda_{P_{Mx}}$ as V varies from 80 to 1000 (m/s) is depicted in Figure 33. The figure shows the outer closed-loop system is sensitive to the change in V but always stays stable. In other words, the primary control system suppresses flutter instabilities for any air stream velocity even at its lowest relative stability value. Typically, a 15% flutter free margin or more is needed beyond the design envelope for both civil and military aircrafts (Hu et al., 2003). These observations also confirm the fact that controlled systems designed based on the LQR principle have very good stability robustness properties (Chen, 2015).
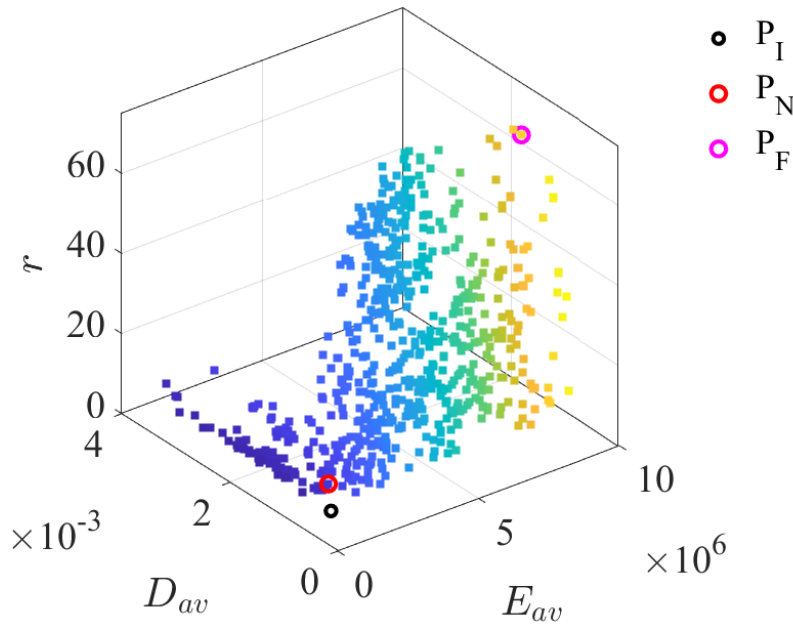

Figure 20: *3D visualization of the Pareto front. The color code indicates the value of the objective function E_{av}. Red denotes the highest value, and dark blue denotes the smallest value. P_I, P_N, and P_F are the ideal, knee, and far point, respectively.*

Figure 21: *Projection #1 of the Pareto set. The color code indicates the value of E_c. Red denotes the highest value, and dark blue denotes the smallest value*
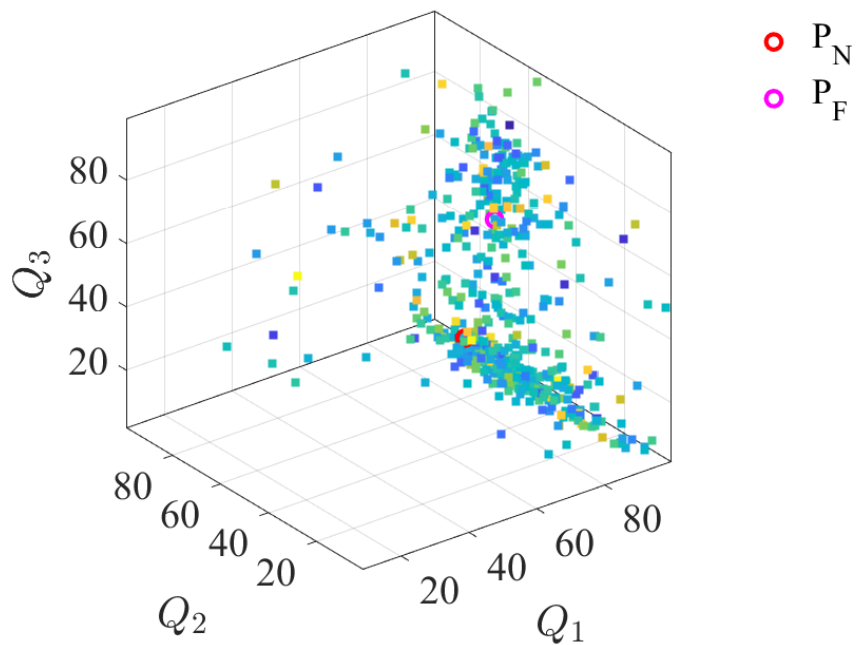
Figure 22: *Projection #2 of the Pareto set. The color code indicates the value of Q_4. Red denotes the highest value, and dark blue denotes the smallest value.*
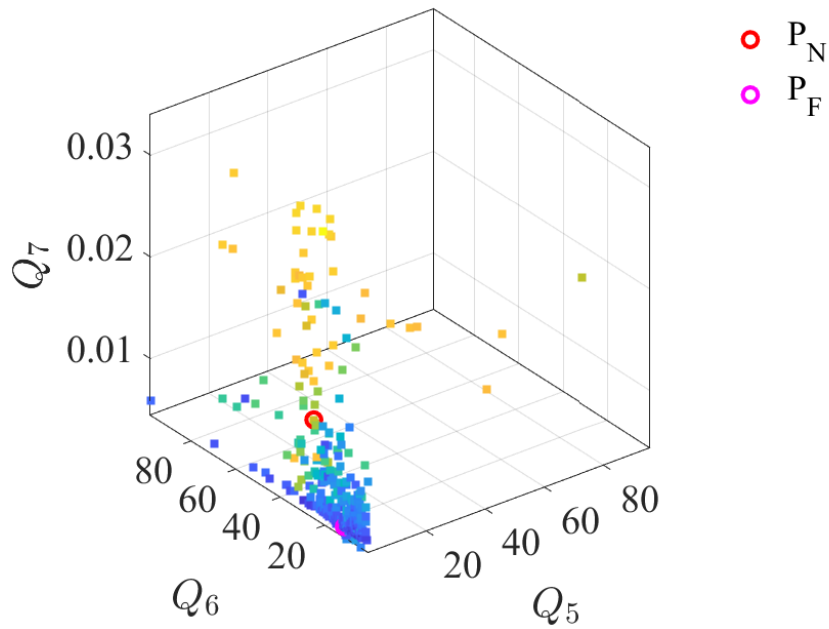
Figure 23: *Projection #3 of the Pareto set. The color code indicates the value of Q_8. Red denotes the highest value, and dark blue denotes the smallest value.*
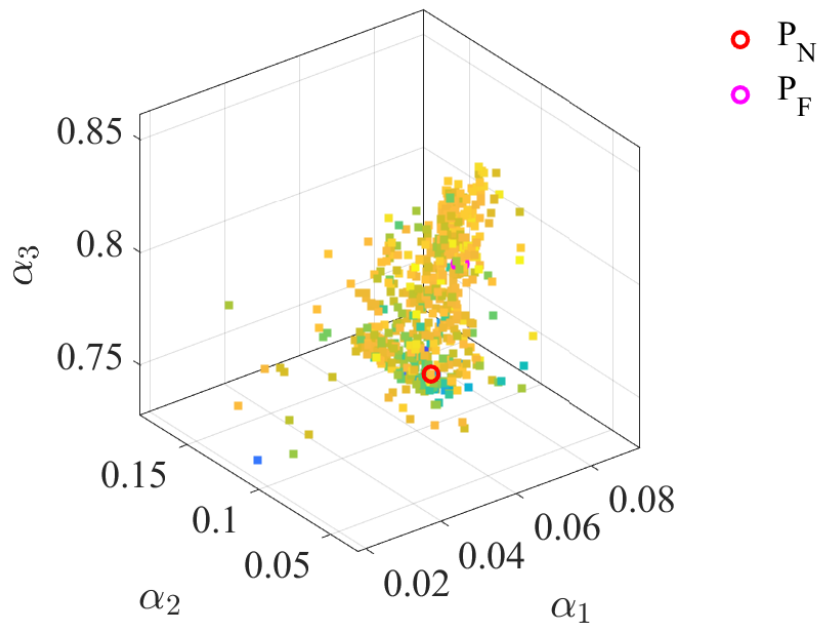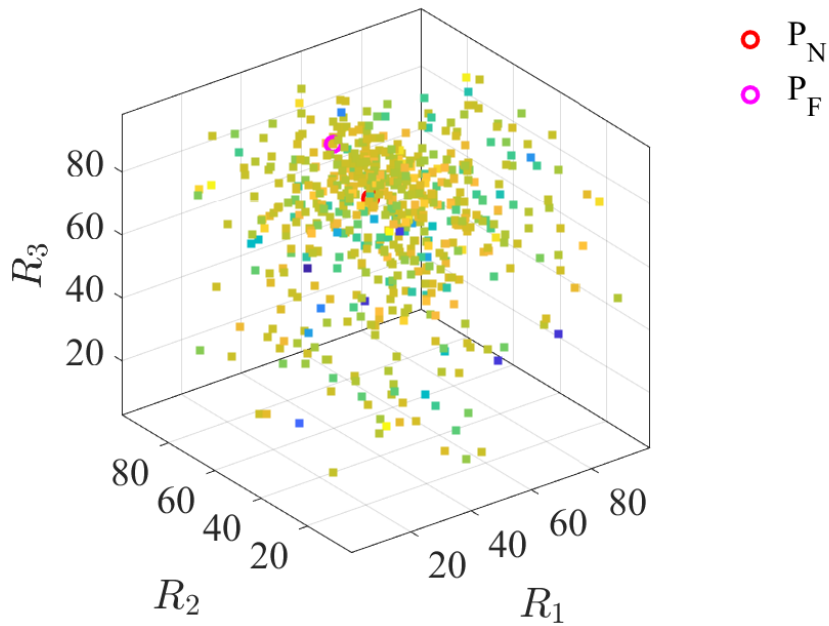

Figure 24: *Projection #4 of the Pareto set. The color code indicates the value of R_4. Red denotes the highest value, and dark blue denotes the smallest value.*
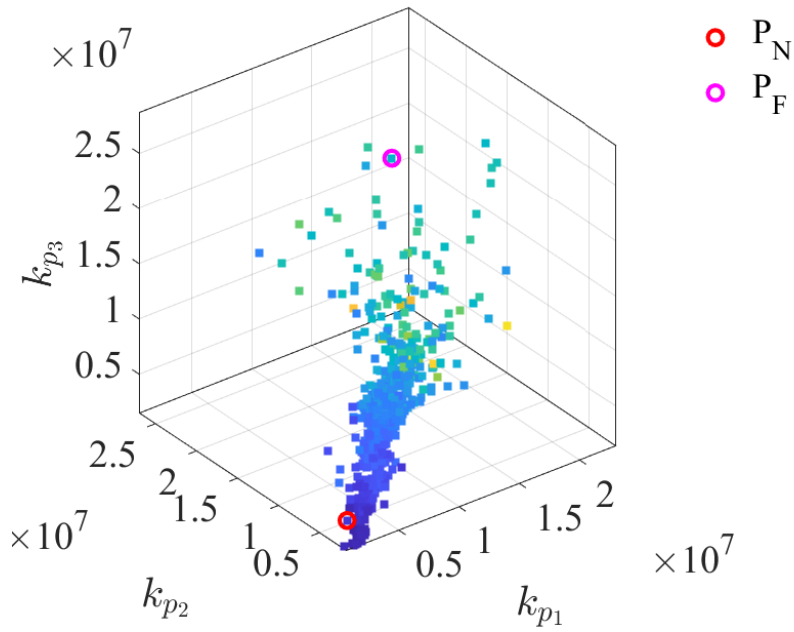
Figure 25: *Projection #5 of the Pareto set. The color code indicates the value of k_{p_4}. Red denotes the highest value, and dark blue denotes the smallest value.*
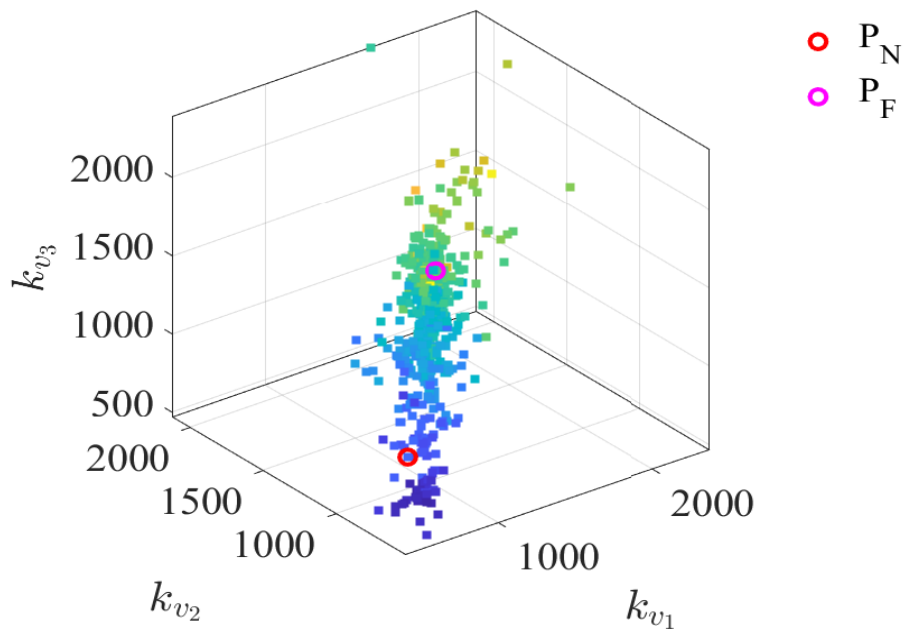
Figure 26: *Projection #6 of the Pareto set. The color code indicates the value of k_{v_4}. Red denotes the highest value, and dark blue denotes the smallest value.*
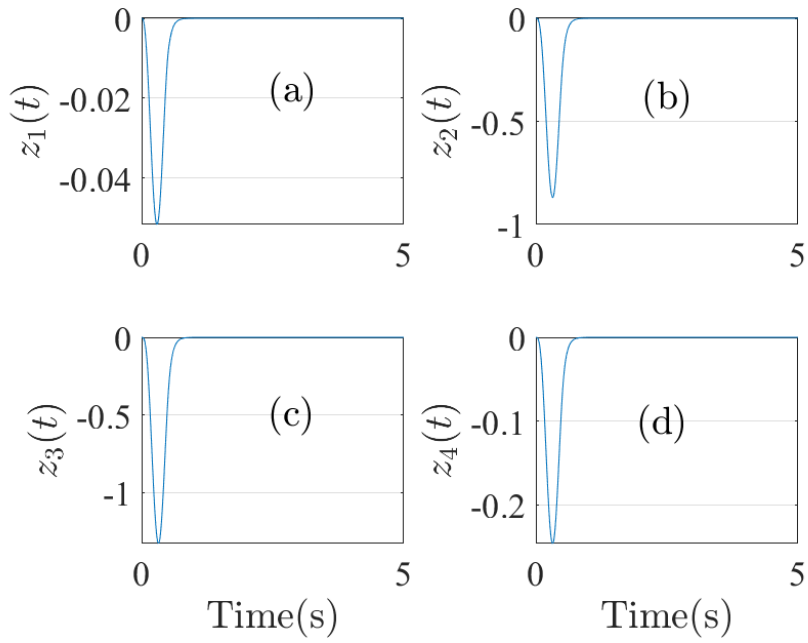
Figure 27: *The response of the outer closed loop system at P_N.*
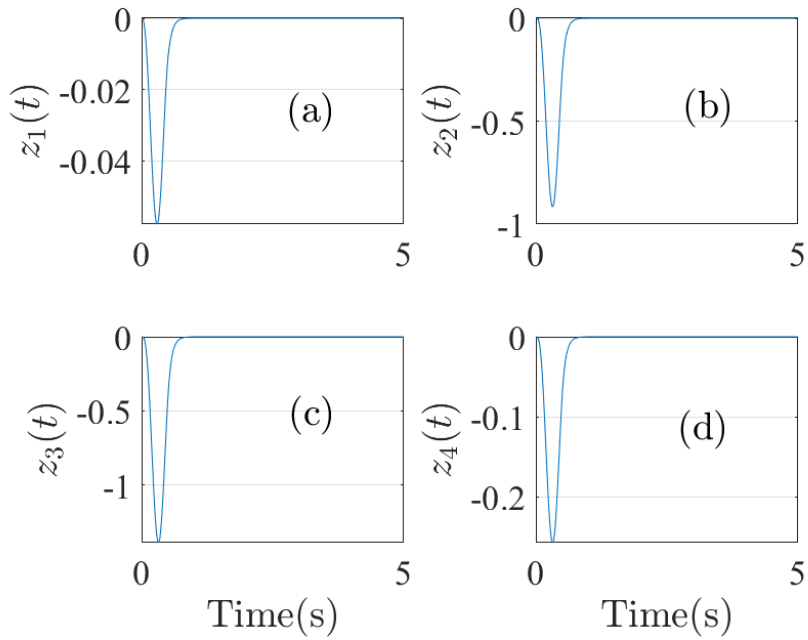
Figure 28: *The response of the outer closed loop system at P_F.*
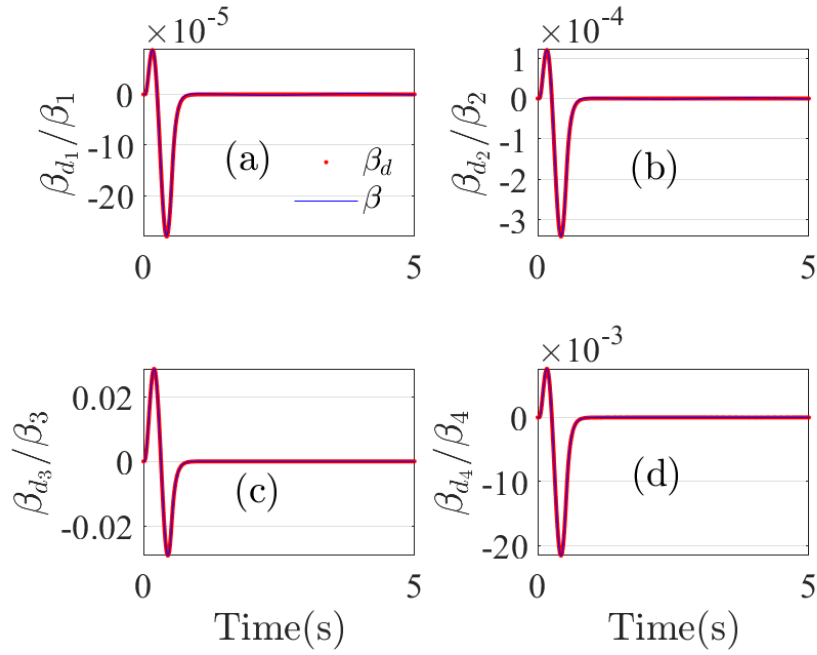
Figure 29: *Tracking performance of the secondary control algorithm at P_N.*
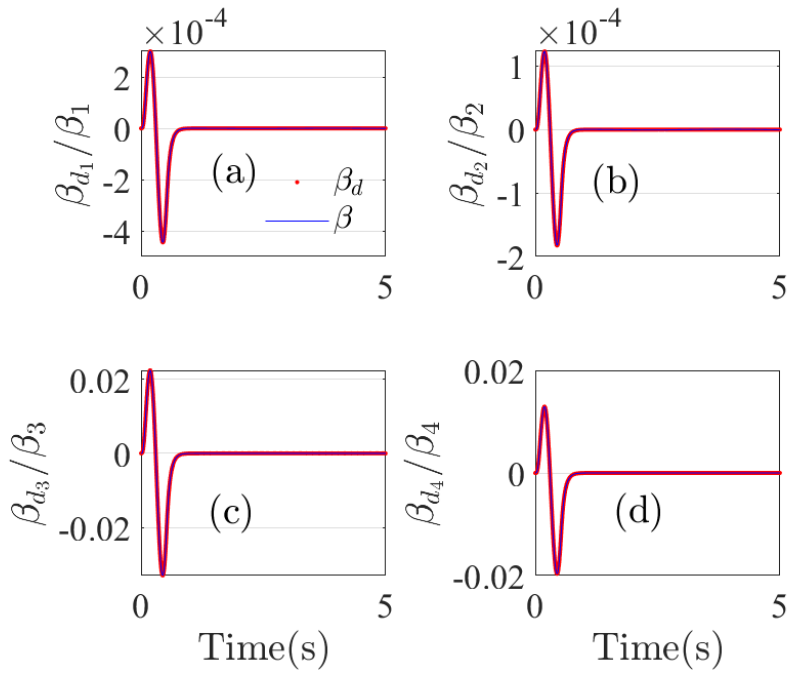
Figure 30: *Tracking performance of the secondary control algorithm at P_F.*
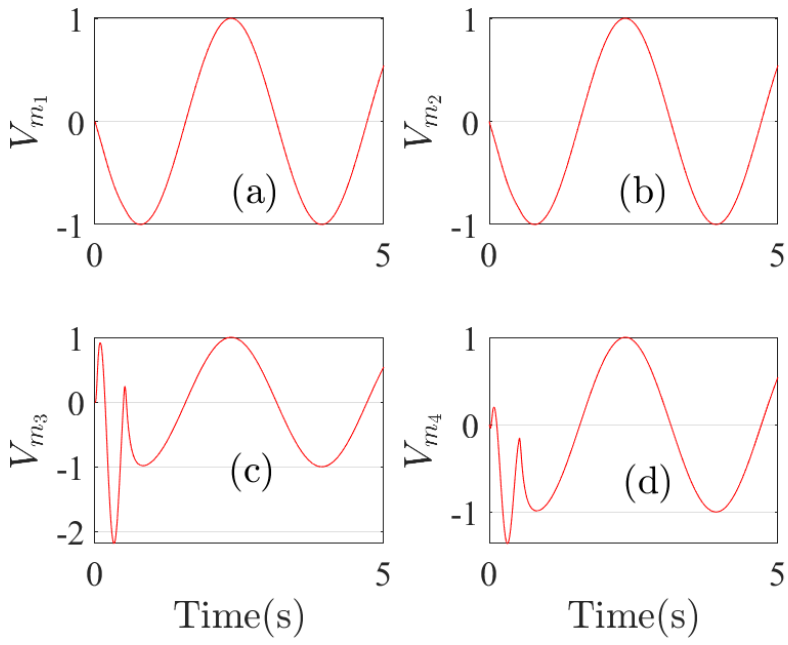
Figure 31: *Voltage signals entering the actuators at P_N.*
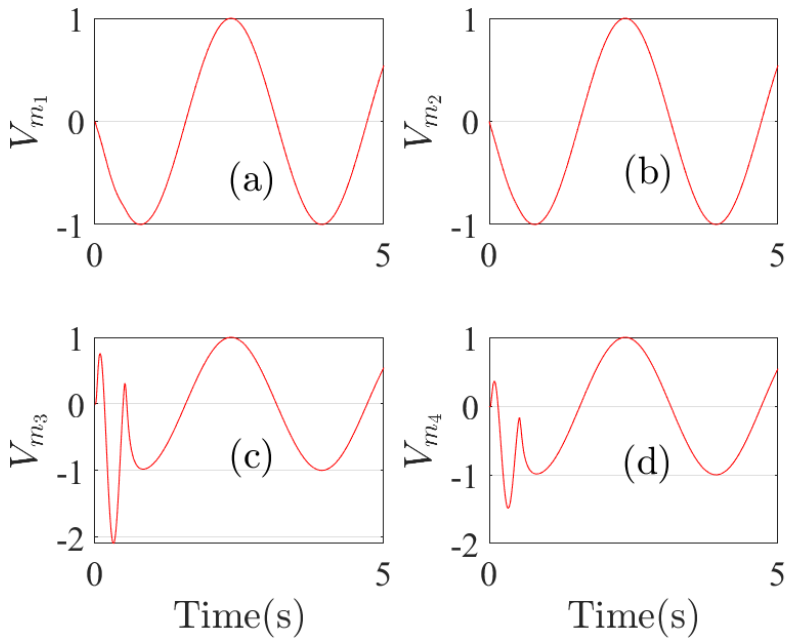
Figure 32: *Voltage signals entering the actuators at P_F.*
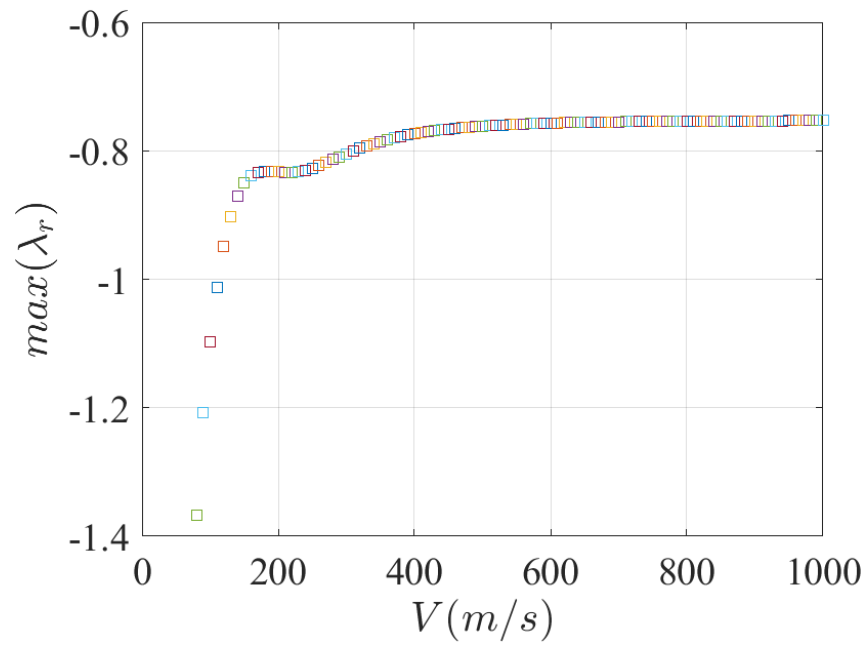
Figure 33: *Profile of λ_r versus V.*

CHAPTER 4: SUMMARY AND FUTURE DIRECTIONS

4.1 Conclusions

We have studied the multidisciplinary and multi-objective optimal design of a cascade control system applied to wing with four control surfaces having actuator dynamics. The optimization problem with 24 design parameters and 3 objective functions is solved by NSGA-II algorithm. The decision variable space consists of 4 parameters related to the span wise and chord lengths of the control surfaces, 12 setup gains related to the LQR penalty matrices, and 8 gains belong to the inner control loops. The objective space contains three objectives: minimization of the controlled system response to gust loads acting on the wing and internal disturbance acting on the actuators, and maximization of speed ratio between the auxiliary and main control loops, and minimization of the control energy utilization. The optimal trade-off solutions in terms of the Pareto set and front are obtained. The Pareto set includes multiple design options from which the decision-maker can choose to implement. The Pareto front demonstrate the competing nature between the design objectives. This conflicting nature can be also seen from the closed-loop system response at selected design points. The profiles of the inner and outer system states show that the secondary controlled is fast enough to prevent internal upsets from spreading to the outer control.

Future studies will focus on the dynamics of the ball-screw and slider-crank mechanisms and their impact on the closed-loop performance. The addition of adding a leading edge and the cross section of the wing will give more depth to the tunable physical parameters.

REFERENCES

Ahuja, V., & Hartfield, R. (2010). Optimization of UAV Designs for Aerodynamic Performance Using Genetic Algorithms. *AIAA/ASME/ASCE/AHS/ASC Structures, Structural Dynamics, and Materials Conference 18th AIAA/ASME/AHS Adaptive Structures Conference*, (p. 2759).

Beyer, H. G., & Deb, K. (2001). On self-adaptive features in real-parameter evolutionary algorithms. *IEEE Transactions on evolutionary computation, 5*(3), 250-270.

Bolton, W. (2015). Instrumentation and control systems. *Newnes*.

Boopathy, K., Rumpfkeil, M., & Kolonay, R. (2015). Robust optimization of a wing under structural and material uncertainties. *17th AIAA Non-Deterministic Approaches Conference*, (p. 0920).

Brown, R. N., & Singh, K. V. (2015). Optimal Sizing and Configurations of the Control Surfaces for Active Aeroelastic Control. *AIAA Atmospheric Flight Mechanics Conference*, (p. 2241).

Brown, R. N.; Singh, K. V.; Kolonay, R. M. (2017). Optimal Sizing and Placement of Control Surfaces for Active Aeroservoelastic Control. *AIAA/ASCE/AHS/ASC Structures, Structural Dynamics, and Materials Conference*, (p. 0569).

Bryson, A. E. (2018). *Applied optimal control: optimization, estimation and control.* Routledge.

Carey, S., & Buttrill, S. (1996). *Aeroservoelastic Simulation of an Active Flexible Wing Wind Tunnel Model.* NASA Langley Technical Report Server.

Chen, C. (2015). *On the robustness of the linear quadratic regulator via perturbation analysis of the Riccati equation.* Dublin City University: Doctoral dissertation.

Corripio, A. (2000). Tuning of industrial control systems. *Isa*.

Deb, K., & Agrawal, R. B. (1995). Simulated binary crossover for continuous search space. *Complex systems, 9*(2), 115-148.

Deb, K., Pratap, A., Agarwal, S., & Meyarivan, T. A. (2002). A fast and elitist multiobjective genetic algorithm: NSGA-II. *IEEE transactions on evolutionary computation, 6*(2), 182-197.

Durillo, J. J., Nebro, A. J., Coello, C. A., García-Nieto, J., Luna, F., & Alba, E. (2010). A study of multiobjective metaheuristics when solving parameter scalable problems. *IEEE Transactions on Evolutionary Computation, 14*(4), 618-635.

Durillo, J. J., Nebro, A. J., Coello, C. A., Luna, F., & Alba, E. (2008). A comparative study of the effect of parameter scalability in multi-objective metaheuristics. *IEEE Congress on Evolutionary Computation (IEEE World Congress on Computational Intelligence)*, (pp. 1893-1900).

El Hajjaji, A., & Ouladsine, M. (2001). Modeling and nonlinear control of magnetic levitation systems. *IEEE Transactions on industrial Electronics, 48*(4), 831-838.

Habibi, S., Jeff, R., & Greg, L. (2008). Inner-loop control for electromechanical (EMA) flight surface actuation systems. *Journal of dynamic systems, measurement, and control ,* 130(5), 051002.

Haghighat, S., Martins, J. R., & Liu, H. H. (2012). Aeroservoelastic design optimization of a flexible wing. Journal of Aircraft. *49*(2), 432-443.

Haupt, R. L., & Ellen Haupt, S. (2004). *Practical genetic algorithms.* John Wiley & Sons,.

Hu, X., Huang, Z., & Wang, Z. (2003). Hybridization of the multi-objective evolutionary

    algorithms and the gradient-based algorithms. *In The 2003 Congress on Evolutionary*

    Computation, 2003. CEC'03, Vol. 2, 870-877.

Ishibuchi, H. Y. (2009). Evolutionary many-objective optimization by NSGA-II and MOEA/D

    with large populations. *IEEE International Conference on Systems, Man and*

    Cybernetics, 1758-1763.

Jackson, T., & Livne, E. (2014). Integrated aeroservoelastic design optimization of actively

    controlled strain-actuated flight vehicles. *AIAA journal*, 1105-1123.

Jones, D. F., Mirrazavi, S. K., & Tamiz, M. (2002). Multi-objective meta-heuristics: An

    overview of the current state-of-the-art. *European journal of operational research,*

    137(1), 1-9.

Kakde, M. R. (2004). Survey on multiobjective evolutionary and real coded genetic algorithms.

    In Proceedings of the 8th Asia Pacific symposium on intelligent and evolutionary

    systems, (pp. 150-161).

Karpel, M., & Sheena, Z. (1989). Structural optimization for aeroelastic control effectiveness.

    Journal of Aircraft, 493-495.

Khot, N. S., Appa, K., & Eastep, F. E. (2000). Optimization of flexible wing without ailerons for

    rolling maneuver. *Journal of aircraft*, 892-897.

Kim, Y., Jeon, Y., & Lee, D. (2006). Multi-objective and multidisciplinary design optimization

    of supersonic fighter wing. *Journal of aircraft*, 817-824.

Kumar, C. A., Nair, N., Begum, S., & Tharani, T. (2012). Multi-objective Cascade Control of

    Regulatory Process with Two Conflicting Objectives. *Procedia engineering, 38*, 4057-

    4063.

Kumar, V. S., Laura, A. M., Raymond, K., & Jonathan, E. C. (2012). Receptance Based Active

    Aeroelastic Control Using Multiple Control. *53rd AIAA/ASME/ASCE/AHS/ASC*

    Structures, Structural Dynamics, and Materials Conference. Honolulu, Hawaii: AIAA

    Paper.

Livne, E. (1999). Integrated aeroservoelastic optimization: status and direction. *Journal of*

    Aircraft, 122-145.

Luenberger, D. G. (1964). Observing the state of a linear system. *IEEE transactions on military*

    electronics, 74-80.

Marler, R. T., & Arora, J. S. (2004). Survey of multi-objective optimization methods for

    engineering. *Structural and multidisciplinary optimization, 26*(6), 369-395.

MathWork. (2020, 07 15). *Pole Placement*. Retrieved from MathWork:

    https://www.mathworks.com/help/control/getstart/pole-placement.html#f2-1031415.

Nam, C., Chattopadhyay, A., & Kim, Y. (2000). Optimal wing planform design for aeroelastic

    control. *AIAA journal*, 1465-1470.

Nikbay, M., & Acar, P. (2012). Flutter based aeroelastic optimization of an aircraft wing with

    analytical approach. *AIAA/ASMEASCE/AHS/ASC Structures, Structural Dynamics and*

    Materials Conference 20th AIAA/ASME/AHS Adaptive Structures Conference, (p. 1796).

Oral, Ö., Çetin, L., & and Uyar, E. (2010). A Novel Method on Selection of Q And R Matrices

    In The Theory Of Optimal Control. *International Journal of Systems Control, 1*(2).

Pareto, V. (1971). Manual of political economy.

Pettit, C., & Grandhi, R. (2003). Optimization of a wing structure for gust response and aileron

    effectiveness. *Journal of aircraft*, 1185-1191.

Qiao, G., Liu, G., Shi, Z., Wang, Y., Ma, S., & Lim, T. (2018). A review of electromechanical actuators for More/All Electric aircraft. *Proceedings of the Institution of Mechanical Engineers, Part C: Journal of Mechanical Engineering Science*, 4128-4151.

Sardahi, Y. (2016). Multi-objective optimal design of control systems. *Doctoral dissertation, UC Merced*.

Sardahi, Y., & Boker, A. (2018). Multi-objective optimal design of four-parameter PID controls. *In ASME 2018 Dynamic Systems and Control Conference. American Society of Mechanical Engineers Digital Collection*, pp.V001T01A001–V001T01A001.

Sardahi, Y., & Sun, J. (2017). Many-objective optimal design of sliding mode controls. *Journal of Dynamic Systems, Measurement, and Control*, 139(1), 014501.

Shibuchi, H., Sakane, Y., Tsukamoto, N., & Nojima, Y. (2009). Evolutionary many-objective optimization by NSGA-II and MOEA/D with large populations. *IEEE International Conference on Systems, Man and Cybernetics*, (pp. 1758-1763).

Singh, K. V., & McDonough, L. A. (2014). Optimization of Control Surface Parameters with Augmented Flutter Boundary Constraints. 2050.

Singh, K. V., Brown, R. N., & Kolonay, R. (2016). Receptance-based active aeroelastic control with embedded control surfaces having actuator dynamics. *Journal of Aircraft, 0*, 830-845.

Singh, K. V., McDonough, L. A., Kolonay, R., & Cooper, J. E. (2014). Receptance-based active aeroelastic control using multiple control surfaces. *Journal of Aircraft*, 113-136.

Smith, C. A., & Corripio, A. B. (1985). *(1985). Principles and practice of automatic process control* (Vol. 2). New York: Wiley.

Srinivas, N., & Deb, K. (1994). Muiltiobjective optimization using nondominated sorting in genetic algorithms. *Evolutionary computation, 2*(3), 221-248.

Stanford, B. K. (2016). Optimization of an aeroservoelastic wing with distributed multiple control surfaces. *Journal of Aircraft*, 1470.

Tewari, A. (2002). Modern control design. In A. Tewari, *Modern control design* (pp. 283-308). NY: John Wiley & sons.

Tian, Y., Cheng, R., Zhang, X., & Jin, Y. (2017). PlatEMO: A MATLAB platform for evolutionary multi-objective optimization [educational forum]. *IEEE Computational Intelligence Magazine, 12*(4), 73-87.

Vio, G., & Cooper, J. (2008). Optimisation of Composite Structures for Aeroelastic Applications Using Evolutionary Algorithms. *AIAA/ASME/ASCE/AHS/ASC Structures, Structural Dynamics, and Materials Conference, 16th AIAA/ASME/AHS Adaptive Structures Conference*, (p. 1972).

Woźniak, P. (2010, December). Multi-objective control systems design with criteria reduction. *In Asia-Pacific Conference on Simulated Evolution and Learning*, 583-587.

Xu, X., Sardahi, Y., & Zheng, C. (2018). Multi-Objective Optimal Design of Passive Suspension System With Inerter Damper. *In ASME 2018 Dynamic Systems and Control Conference. American Society of Mechanical Engineers Digital Collection.*, pp. V003T40A006–V003T40A006.

Zhang, J., & Zhou, J. (2017). Design and optimization of an adjustable electromechanical actuator. *IEEE 3rd Information Technology and Mechatronics Engineering Conference*, (pp. 272-275).

APPENDIX A: LETTER OF APPROVAL

MARSHALL UNIVERSITY®
www.marshall.edu

Office of Research Integrity

November 30, 2020

Christopher Greer
208 Whitney Lane
Bristol, TN 37620

Dear Mr. Greer:

This letter is in response to the submitted thesis abstract entitled *"Multidisciplinary and Multi-Objective Optimal Design of a Cascade Control System for a Flexible Wing with Embedded Control Surfaces Having Actuator Dynamics."* After assessing the abstract, it has been deemed not to be human subject research and therefore exempt from oversight of the Marshall University Institutional Review Board (IRB). The Code of Federal Regulations (45CFR46) has set forth the criteria utilized in making this determination. Since the information in this study does not involve human subjects as defined in the above referenced instruction, it is not considered human subject research. If there are any changes to the abstract you provided then you would need to resubmit that information to the Office of Research Integrity for review and a determination.

I appreciate your willingness to submit the abstract for determination. Please feel free to contact the Office of Research Integrity if you have any questions regarding future protocols that may require IRB review.

Sincerely,

Bruce F. Day, ThD, CIP
Director

WE ARE... MARSHALL.
One John Marshall Drive • Huntington, West Virginia 25755 • Tel 304/696-4303
A State University of West Virginia • An Affirmative Action/Equal Opportunity Employer

APPENDIX B

B.1. Electromagnetic Actuator

The EMA shown in Figure 15 (see chapter 3) is described by the following equations

$$G_e = \frac{1/R_c}{\frac{L_c}{R_c s}+1} = \frac{1/R_c}{\tau_e s+1},$$ (B.1)

τ_e and $1/R_c$ are the motor's electrical time constant and gain. Assuming the inductance is very

small ($L_c = 0 \to \tau_e = 0$), which is the case in many inductive loads. The motor's dynamics can

be reduced to the following transfer function

$$G_e=1/R_c.$$ (B.2)

The transfer function of the mechanical part of the motor (motor shaft and gearbox) is

approximated by G_{mech} such that

$$G_{mech} = \frac{1/K_{mv}}{\frac{J_m}{K_{mv}}s+1} = \frac{K_m}{\tau_m s+1},$$ (B.3)

Definitions and values of some of the parameters used in the computer simulations are

tabulated in Table 2.

Table 2: Motor parameters (Habibi et al., 2008).

Symbol	Definition	Value
J_m	Rotor inertia	0.000391, lb $in.^2$
K_c	Torque constant	2.376, in.lb/A
K_{mv}	Viscous friction and damping	0.00116, in.lb s/rad
K_ω	Back emf constant	0.1342, V s/rad
R_c	Winding resistance	2.12,Ω
τ_m	*Mechanical time constant*	0.3371, s

B.2. Slider-Crank Mechanism

The kinematic equations of the slider-crank mechanism in Figure 16 (see chapter 3) read

Knowing that $\sin \Phi^2 + \cos \Phi^2 = 1$, $\cos \Phi^2 = 1 - \sin \Phi^2$, $\cos \Phi = \sqrt{1 - \sin \Phi^2}$ and setting

$n = \frac{b}{a}$, we notice that $\sin \Phi = \frac{\sin \beta}{n}$. After few steps of mathematical substitutions and simplifications, the relationship between the rack-pinion displacement X and slider-crank angular displacement β can be found as follows

$$\cos \Phi = \sqrt{1 - \sin \Phi^2} = \sqrt{1 - \frac{\sin \beta^2}{n^2}} \tag{B.4}$$

$$X = a \left[n \left(1 - \sqrt{1 - \frac{\sin \beta^2}{n^2}} \right) + (1 - \cos \beta) \right] \tag{B.5}$$

$$\frac{X}{a} = \left[n \left(1 - \sqrt{1 - \frac{\sin \beta^2}{n^2}} \right) + (1 - \cos \beta) \right] \tag{B.6}$$

$$\frac{X}{a} = n - n\sqrt{1 - \frac{\sin \beta^2}{n^2}} + 1 - \cos \beta \tag{B.7}$$

$$\frac{X}{a} = n - n\sqrt{\frac{n^2 - \sin \beta^2}{n^2}} + 1 - \cos \beta \tag{B.8}$$

$$\frac{X}{a} = n - \sqrt{n^2 - \sin \beta^2} + 1 - \cos \beta \tag{B.9}$$

$$\frac{X}{a} - n - 1 = -\sqrt{n^2 - \sin \beta^2} - \cos \beta \tag{B.10}$$

$$\sqrt{n^2 - \sin \beta^2} + \cos \beta = 1 + n - \frac{X}{a} \tag{B.11}$$

now, $\sin \beta^2 + \cos \beta^2 = 1 \qquad \sin \beta^2 = 1 - \cos \beta^2 \tag{B.12}$

$$\sqrt{n^2 - 1 + \cos \beta^2} + \cos \beta = 1 + n - \frac{X}{a} \tag{B.13}$$

$$\begin{cases} A = \cos \beta \\ B = 1 + n - \frac{X}{a} \end{cases} \tag{B.14}$$

$$\sqrt{n^2 - 1 + A^2} + A = B \tag{B.15}$$

$$n^2 - 1 + A^2 = B^2 + A^2 - 2AB \tag{B.16}$$

68

$$A = \frac{B^2 - n^2 + 1}{2B} \tag{B.17}$$

$$\cos\beta = \frac{(1+n-\frac{X}{a})^2 - n^2 + 1}{2\ (1+n-\frac{X}{a})} \tag{B.18}$$

$$\beta = \arccos\frac{(1+n-\frac{X}{a})^2 - n^2 + 1}{2\ (1+n-\frac{X}{a})} \tag{B.19}$$

APPENDIX C

C.1.   Wing having three control surfaces.

According to Kumar, Laura, Raymond, and Jonathan (2012), the parameters and matrices for the

system given in Eq. (1) are as follows:

$$\bar{c} = \left(\frac{c^2}{2} - cx_f\right), \tilde{c} = \left(\frac{c^3}{3} - c^2 x_f + cx_f^2\right), e_d = \sqrt{E_c(1 - E_c)} ,$$

$$b_c = a_w/\pi(1 - E_c)e_d, \qquad a_c = a_w/\pi(\cos^{-1}(1 - E_c) + 2e_d)$$

$$M = m\begin{bmatrix} \bar{s}^5 c/5 & \bar{s}^6 c/6 & \bar{s}^4 \bar{c}/4 & \bar{s}^5 \tilde{c}/5 \\ \bar{s}^6 c/6 & \bar{s}^7 c/7 & \bar{s}^5 c\bar{c}/5 & \bar{s}^6 c\bar{c}/6 \\ \bar{s}^4 \bar{c}/4 & \bar{s}^5 \bar{c}/5 & \bar{s}^3 \tilde{c}/3 & \bar{s}^4 \tilde{c}/4 \\ \bar{s}^5 \tilde{c}/5 & \bar{s}^6 \tilde{c}/6 & \bar{s}^4 \tilde{c}/4 & \bar{s}^5 \tilde{c}/5 \end{bmatrix}$$

$$C_a = \begin{bmatrix} -ca_w \bar{s}^5/10 & -ca_w \bar{s}^6/12 & 0 & 0 \\ -ca_w \bar{s}^6/12 & -ca_w \bar{s}^7/14 & 0 & 0 \\ -c^2 ea_w \bar{s}^4/8 & c^2 ea_w \bar{s}^5/10 & c^3 M_{\dot{\theta}} \bar{s}^3/24 & c^3 M_{\dot{\theta}} \bar{s}^4/32 \\ -c^2 ea_w \bar{s}^5/10 & c^2 ea_w \bar{s}^6/12 & c^3 M_{\dot{\theta}} \bar{s}^4/32 & c^3 M_{\dot{\theta}} \bar{s}^5/40 \end{bmatrix}$$

$$K = \begin{bmatrix} 4EI\bar{s} & 6EI\bar{s}^2 & 0 & 0 \\ 6EI\bar{s}^2 & 12EI\bar{s}^3 & 0 & 0 \\ 0 & 0 & GJ\bar{s} & GJ\bar{s}^2 \\ 0 & 0 & GJ\bar{s}^2 & 4GJ\bar{s}^3/3 \end{bmatrix}$$

$$K_a = \begin{bmatrix} 0 & 0 & -ca_w \bar{s}^4/8 & -ca_w \bar{s}^5/10 \\ 0 & 0 & -ca_w \bar{s}^5/10 & -ca_w \bar{s}^6/12 \\ 0 & 0 & c^2 ea_w \bar{s}^3/6 & c^2 ea_w \bar{s}^4/8 \\ 0 & 0 & c^2 ea_w \bar{s}^4/8 & c^2 ea_w \bar{s}^5/10 \end{bmatrix}$$

$$F_c = \rho V^2 c \begin{bmatrix} -a_c s_1^3/6 & -a_c(s_2^3 - s_1^3)/6 & -a_c(\bar{s}^3 - s_2^3)/6 \\ -a_c s_1^4/8 & -a_c(s_2^4 - s_1^4)/8 & -a_c(\bar{s}^4 - s_2^4)/8 \\ cb_c s_1^2/4 & cb_c(s_2^2 - s_1^2)/4 & cb_c(\bar{s}^2 - s_2^2)/4 \\ cb_c s_1^3/6 & cb_c(s_2^3 - s_1^3)/6 & cb_c(\bar{s}^3 - s_2^3)/6 \end{bmatrix}$$

$$F_g = \rho V c \begin{bmatrix} -a_c s_1^3/6 & -a_w(s_2^3 - s_1^3)/6 & -a_w(\bar{s}^3 - s_2^3)/6 \\ -a_c s_1^4/8 & -a_w(s_2^4 - s_1^4)/8 & -a_w(\bar{s}^4 - s_2^4)/8 \\ ces_1^2/4 & ce(s_2^2 - s_1^2)/4 & ce(\bar{s}^2 - s_2^2)/4 \\ ces_1^3/6 & ce(s_2^3 - s_1^3)/6 & ce(\bar{s}^3 - s_2^3)/6 \end{bmatrix}$$

Table 3: *Aeroelastic system parameters for the wing having three control surfaces*

Parameter	Symbol	Value
Semi-span (m)	$\bar{s}$	6
Chord (m)	c	1
Mass per unit area (kg/m^2)	m	10
Air density (kg/m^3)	ρ	1.225
2D lift curve slope	a_w	2π
Unsteady torsional velocity term	$M_{\dot\theta}$	1.2
Eccentricity ratio	e	0.15
Position of flexural axis	x_f	$0.4c$
Flexural rigidity	EI	400×10^3
Torsional rigidity	GJ	200×10^3

For the aircraft's wing with four control surfaces described by Eq. (29), $\boldsymbol{F_c}$, $\boldsymbol{F_g}$, and the system

parameters are given by:

$$
\boldsymbol{F_c} = \rho V^2 c
\begin{bmatrix}
-a_c s_1^3/6 & -a_c(s_2^3 - s_1^3)/6 & -a_c(s_3^3 - s_2^3)/6 & -a_c(\bar{s}^3 - s_3^3)/6 \\
-a_c s_1^4/8 & -a_c(s_2^4 - s_1^4)/8 & -a_c(s_3^4 - s_2^4)/8 & -a_c(\bar{s}^4 - s_3^4)/8 \\
cb_c s_1^2/4 & cb_c(s_2^2 - s_1^2)/4 & cb_c(s_3^2 - s_2^2)/4 & cb_c(\bar{s}^2 - s_3^2)/4 \\
cb_c s_1^3/6 & cb_c(s_2^3 - s_1^3)/6 & cb_c(s_3^3 - s_2^3)/6 & cb_c(\bar{s}^3 - s_3^3)/6
\end{bmatrix}
$$

$$
\boldsymbol{F_g} = \rho V c
\begin{bmatrix}
-a_c s_1^3/6 & -a_w(s_2^3 - s_1^3)/6 & -a_w(s_3^3 - s_2^3)/6 & -a_w(\bar{s}^3 - s_3^3)/6 \\
-a_c s_1^4/8 & -a_w(s_2^4 - s_1^4)/8 & -a_w(s_3^4 - s_2^4)/8 & -a_w(\bar{s}^4 - s_3^4)/8 \\
ces_1^2/4 & ce(s_2^2 - s_1^2)/4 & ce(s_3^2 - s_2^2)/4 & ce(\bar{s}^2 - s_3^2)/4 \\
ces_1^3/6 & ce(s_2^3 - s_1^3)/6 & ce(s_3^3 - s_2^3)/6 & ce(\bar{s}^3 - s_3^3)/6
\end{bmatrix}
$$

Table 4: *Aeroelastic system parameters for the wing having four control surfaces*

Parameter	Symbol	Value
Semi-span (m)	$\bar{s}$	10
Chord (m)	c	1
Mass per unit area (kg/m^2)	m	10
Air density (kg/m^3)	ρ	1.225
2D lift curve slope	a_w	2π
Unsteady torsional velocity term	$M_{\dot{\theta}}$	1.2
Eccentricity ratio	e	0.25
Position of flexural axis	x_f	$0.5c$
Flexural rigidity	EI	4×10^6
Torsional rigidity	GJ	2×10^5